Summer 2024

Development and Testing of High Strength Scalable High Entropy Alloys

Hans Jakob Pommerenke
Missouri University of Science and Technology

Department: Materials Science and Engineering

DEVELOPMENT AND TESTING OF HIGH STRENGTH SCALABLE HIGH ENTROPY ALLOYS

by

HANS JAKOB POMMERENKE

A DISSERTATION

Presented to the Graduate Faculty of the

MISSOURI UNIVERSITY OF SCIENCE AND TECHNOLOGY

In Partial Fulfillment of the Requirements for the Degree

DOCTOR OF PHILOSOPHY

in

MATERIALS SCIENCE AND ENGINEERING

2024

Approved by:

Dr. Haiming Wen, Advisor
Dr. Ronald O'Malley
Dr. Joseph Newkirk
Dr. Yija Gu
Dr. Frank Liou

PUBLICATION DISSERTATION OPTION

This dissertation consists of the following three articles, formatted in the style used by the Missouri University of Science and Technology:

Paper I: Pages 7–28, has been submitted to *Journal of Alloys and Compounds*.

Paper II: Pages 29–54, is intended for submission to *Journal of Alloys and Compounds*.

Paper III: Pages 55–87, is intended for submission to *Journal of Materials Processing Technology*.

ABSTRACT

High entropy alloys have shown promise through their ability to be tailored to specific scenarios. From highly corrosive environments to precipitation strengthened alloys to radiation environments high entropy alloys allow tailor made alloys for every solution. New compositions are developed and tested but little work focuses on the processing effect choosing rather than using processing as a stepping stone to achieve properties without investigating the processing effects. This work focuses on single phase face-centered cubic alloys strengthened by processing and precipitation strengthening. In conjunction with the development of these alloys, the ability to scale production will be investigated and characterized to determine major hurdles for future work. FeNiMn30Cr10, FeNiMn20Cr20, FeNiMn20Cr20 Ti2Al1 and FeNiMn20Cr20 Ti1Al3 are investigated for their mechanical properties, their precipitation behavior where applicable, and the effects of various processes on each of the alloys to improve performance or understand potential future pitfalls for production. FeNiMn20Cr20 Ti1Al3 was found to have the most favorable properties with a peak aged strength of 890 MPa at an elongation of 45%. The process of casting this alloy in a small scale foundry was investigated and the effect of contaminates in the form of inclusions were also looked at. It was determined that the different processing steps are such as homogenization and even aging are vital for inclusion elimination.

ACKNOWLEDGMENTS

First and foremost, I thank and am appreciative of my PhD advisor Dr. Haiming Wen. He has given me advice, opportunities, funding, and the tools to be a successful graduate student. Thank you to Dr. Ronald O'Malley, Dr. Frank Liou, Dr. Joseph Newkirk, and Dr Yija Gu for serving on my committee and guiding me. Thank you to Dr. C. Weisner, Dr. M. Buchely, Teneke Hill, and Emily Bullock. Thank you to all my colleagues graduated and still attending Maalavan Arivu, Andrew Hoffman, Matthew Luebbe, Joshua Rittenhouse, and Visharad Jalan. These and many others have made my time as a graduate student a successful and productive time.

TABLE OF CONTENTS

Page

SECTION

LIST OF ILLUSTRATIONS

PAPER I Page

PAPER II

LIST OF TABLES

1. INTRODUCTION

High entropy alloys are a relatively new field really springing forth in the last 20 years. The earliest papers mentioning high entropy alloys (HEAs) or multi-principal element alloys (MPEAs) are generally dated 2004 by Cantor et al. [1] and by Yeh et al [2] The explosion of available data in this field is an amazing sight to see. While the interactions between many different elements can be complex research has shown that many alloys actually create simple phases if not a single phase. [2, 3]These HEAs often are tailor made to specific situations and have properties that can match or outshine those of modern [4–7] All steels are iron based, and while superalloys such as nickel or cobalt based principal element alloys are coming into play more and more, all these alloy types focus on a single element with other alloying elements added to produce certain properties. [8] There are alloys such as FeMnAl and FeCrAl alloys which contain 3 principal elements and the rise of these alloys really suggests that the addition of more principal elements is the direction of the future. [9–11]

1.1. HIGH ENTROPY ALLOY BASICS

Traditionally, high entropy alloys have been considered to be 5 or more principal elements ranging from 5-35%.[12] Often though, the definition is expanded to include 4 or more principal elements. This is also why the term multi-principal element alloys has arisen, to provide an umbrella term for this new emerging field. The novelty of high entropy alloys comes from 4 main concepts. These concepts are: the high entropy effect, the lattice distortion effect, the sluggish diffusion effect, and the ‘cocktail’ effect. [12, 13]

Each of these effects plays an important role in the reason for the research dedicated the field of high entropy alloys.

The high entropy effect is an effect based on the energies of formation of phases. While it may not apply to all high entropy alloys equally, simple phases are energetically favorable often resulting in single phase systems. [2, 3] The contest between different formation energies results in generally simple phases, though often, these energies are not quantitatively defined, rather, due to the complexity of the systems, energies are qualitatively defined and ranked in comparison to each other.[3]

The lattice distortion effect is the effect of multiple elements taking up position in a lattice. Each of these lattice sites theoretically have a fixed distance from other lattice sites but due to the mismatch in size of the atoms of different elements, these positions may shift. This mismatch leads to more possibilities of positions for each individual atom known as configurational entropy as well as an internal strain to the lattice structure. [14–16]

Sluggish diffusion, while seen as a major tenant in defining high entropy alloys, has also been questioned. Sluggish diffusion as an effect suggests that due to higher internal strain in the lattice and the higher entropy the individual atoms will need more energy to move throughout a lattice structure thus making the diffusion more ‘sluggish’.[17] This principal of high entropy alloys though has come under more criticism as studies have begun to show that while some elements may experience more sluggish diffusion, other elements and other systems do not display any sort of sluggish diffusion, going as far as to enhance diffusion for some elements in certain systems. For instance, Li et al. 2017 in showed that for the studied alloy, sluggish diffusion did not apply to all elements.[18] Furthermore Divinksi, 2018 investigated multiple alloys and determined grain

boundary diffusion may be faster while intergranular diffusion may be sluggish. [19] Sluggish diffusion has also been promoted as the source of high temperature stability for some high entropy alloy systems which has also been called into question.[12]

1.2. WHY HIGH ENTROPY ALLOYS

Funding for research into high entropy alloy comes from a diverse range of sources. Most research focuses on the replacement of a more common steel with a tailor-made solution for a specific situation. Applications range from replacing steel in highly corrosive environments such as the oil and gas industry or chemical plants to alloys which require stronger tolerance to radiation damage. With research pushing towards more tailored applications, competition with the steel industry presents an issue for commercialization. Another roadblock to commercialization is production costs. While some industries (i.e., the nuclear industry) have a budget that prioritizes product lifetime and safety, other industries put additional focus on the production costs. As a result, the use of costly metals such as nickel reduces the viability of high entropy alloys in industries with more limited budgets or a larger focus on cost optimization.

For the nuclear industry in specific, safety is a priority. As a result, funds are allocated for materials which can outlast the 316L steel currently used in many aspects of a nuclear reactor. In this regard, the use of high entropy alloys in the nuclear industry has an additional bonus. Due to lattice distortion and theoretical ‘sluggish’ diffusion, high energy alloys are more resistant to damage by radiation.[13, 20, 21] This attribute makes high entropy alloys a advantageous candidates for use in nuclear applications compared to currently used alloys.[22] Funding for this research comes from a variety of sources around

the world including the Nuclear Regulatory Commission, the National Nuclear Laboratory, and European Development Fund.

Although high entropy alloys present several advantages for the nuclear industry, the properties of individual materials must be considered to avoid unwanted reactions. Under certain conditions, cobalt can be activated under irradiation and become radioactive itself. Processing methods must also be considered for specific applications. Current literature does not often address processing methods which are an important step in the commercial production of high entropy alloys.

1.3. PROCESSING

Literature often under explains the use of rolling [23] or the use of heat treatments[24]. Often, literature skips solution treating steps which yield scientifically interesting results but do not necessarily have any basis in real world applications. With this lack of processing and scaling knowledge, a large knowledge gap appears in current literature.

The effect of hot rolling in steels is well known. The effect leads to an equiaxed microstructure with a large spread of data available to estimate strengths. This wealth of knowledge, which was built up over many hundreds of years, is a hallmark of the steel industry. The use of these datasets as a baseline has contributed to the design of high entropy alloys. Due to the complex nature of interactions between different elements in an alloy, the true changes in a new cast material are unknown. Increased data from rolling experiments, as well as from inclusion analysis of cast and material, needs to become available to properly build databases for the correct estimation of properties. [25,26]

Finally, the ‘cocktail’ effect is a summary of properties. The effect draws attention to the complex interactions between different elements.[12] This is the source of many high impact research studies that study the diverse properties of high entropy alloys. This effect lets alloy systems be tailored to specific applications. For instance, high entropy alloys were tailor-made for complex environments such as nuclear reactors and corrosion heavy environments. Additionally, structural high entropy alloys were investigated for high strength, high ductility applications.[27–31]

1.4. PRECIPITATION STRENGTHENING

Precipitation strengthening of alloys uses secondary or tertiary phases to strengthen a material. Strengthening occurs through lattice strain which disruptions the matrix through precipitate. Lattice strain also hinders dislocation movement by precipitates and precipitates acting as dislocation pinning sites. [32] High entropy alloys in literature use a wide variety of different precipitates and secondary phases for their strengthening effects. Qi. et. al. shows that using a Heusler phase on the grain boundaries provides significant strengthening.[5] Others use phases such as $L1_2$ and sigma phases to strengthen the high entropy alloy while maintaining up to 60% ductility.[33,34] For this research, the focus is on two sets of precipitates which are positively correlated with strength, the L_{12} and y’, and one precipitate whose formation is to be avoided, the sigma phase due to its lack of ductility and ability to grow in the matrix. [35] The effects of Ti and Al alloying agents added to the studied alloy vary greatly; thereby, these alloying agents must be added with care. $L1_2$, a precipitate, is also seen as a stably forming precipitate, making it ideal for strengthening.[6] In addition, the $L1_2$ when in the right ratio of Ti and Al forms nano-scale precipitates which enhance the mechanical properties of a given alloy.[36]

1.5. MOVING PAST THE LAB SCALE

While a relatively new field, high entropy alloys often tout properties useful in many different industries often relating to structural alloys as well as specialty alloys for nuclear fields.[37–39] While these properties may be promising, a big hurdle is the scalability of various alloy productions. It is relatively simple to cast small amounts with pure materials in an atmospherically controlled furnace. What is often not considered is that for a structural material the raw materials are often not as pure as can be hoped for, atmosphere in an open induction or arc melting furnace is a flowing argon blanket, slag buildup, inclusions, and a large host of other issues all play into the production of large castings. In addition, the use of complex alloying agents and the so called “cocktail effect” while providing benefits, also can create complex inclusions, slag layers which attack furnace linings, and even provide challenges with temperature control as large amounts of for instance Mn can rapidly lower the temperature of a furnace.

With these issues in mind, while work on projects should continue to design superior alloys for use in industrial application, research and thought should be given to how simple it is to scale up these processes. Without research which looks into the effects of casting in non-perfect conditions, the world of high entropy alloys may reach a funding and feasibility turning point.

PAPER

I. A STRONG AND DUCTILE COBALT-FREE SOLID-SOLUTION $Fe_{30}Ni_{30}Mn_{30}Cr_{10}$ MULTI-PRINCIPAL ELEMENT ALLOY FROM HOT ROLLING

Hans Pommerenke[1], Jiaqi Duan[1,3], Nathan Curtis[1], Victor DeLibera[1], Adam Bratten[1], Andrew Hoffman[1,2], Mario Buchely[1], Ronald O'Malley[1], Haiming Wen[1]*

[1] Department of Materials Science and Engineering, Missouri University of Science and Technology, Rolla, MO 65401, USA

[2] General Electric Global Research Center, Niskayuna, NY 12309, USA

[3] Warwick Manufacturing Group, University of Warwick, Coventry, CV4 7AL, UK

ABSTRACT

Most of the face-centered cubic (FCC) multi-principal element alloys (MPEAs) developed thus far contain cobalt. For many applications, it is either required or beneficial to avoid cobalt, since cobalt has long-term activation issue (for nuclear applications), is expensive, and is considered a critical material. In addition, FCC structured solid-solution MPEAs tend to have relatively low strength. A FCC solid-solution $Fe_{30}Ni_{30}Mn_{30}Cr_{10}$ (at %) MPEA was fabricated via arc melting, followed by homogenization at 1100 °C for 12 h. The alloy was hot rolled at 1100 °C with a total reduction of up to 97 %. The microstructure was characterized and mechanical properties were investigated at various stages. Tensile testing showed that yield strength (YS) increased by 285–595 MPa and ultimate tensile strength (UTS) increased by 520–710 MPa. This increase in YS and UTS occurred with a total elongation (ductility) of 40 %.

Meanwhile, hot rolling at high reductions led to evident decreases in size and area fraction of Mn-rich inclusions. Overall, after hot rolling, this FCC solid-solution MPEA is both strong and ductile.

1. INTRODUCTION

Though a relatively new field with most studies having been performed after 2005, MPEAs show a promise in a wide range of applications, owing to their high ductility, high strength, good corrosion resistance, and a strong resistance to radiation damage [1]. While MPEAs were originally designed and developed as single-phase equimolar alloys, many MPEAs reported more recently are non- equimolar. MPEAs have good properties due to a multitude of effects including the high-entropy effect, i.e., increased phase stability due to the high mixing entropy, which competes with the enthalpy of formation for secondary phases. Sluggish diffusion and lattice distortion also play a large role in stability of MPEAs. Sluggish diffusion is a result of the energy needed to break and form bonds as an atom diffuses throughout the matrix lattice with lattice distortion [2]. The possession of many attractive properties as mentioned earlier make investigation into different MPEAs lucrative as materials for applications in extreme environments such as nuclear reactors.

Nuclear reactors represent extremely harsh environments, owing to the presence of high temperature, high stress, intense irradiation, and corrosion by the coolant. Such environments pose enormous challenges to materials, which constitutes a materials science/engineering challenge. MPEAs have potential for improved performance and

robustness in nuclear reactors, owing to improved stability and mechanical properties as well as enhanced resistance to irradiation [3] and corrosion [4]. For nuclear structural materials and fuel cladding, cobalt needs to be avoided, because of the creation of Co-60, which is very radioactive and has a long half-life. Most of the FCC structured MPEAs developed thus far contain Co, whereas only an extremely small number of FCC Co-free MPEAs have been reported [4], [5], [6]. A Co-free $Fe_{27}Ni_{28}Mn_{27}Cr_{18}$ MPEA (cold rolled) has been reported to possess an ultimate tensile strength (UTS) of ~630 MPa [5] with a total elongation (ductility) of ~37 % at room temperature; this alloy also exhibited good irradiation damage resistance [6]. Another Co-free $Fe_{40}Ni_{20}Mn_{20}Cr_{20}$ MPEA (cold rolled followed by annealing) exhibited an UTS of 1.34 GPa and total elongation of 23 % at cryogenic temperature of 77 K [7]; however, this MPEA had an UTS of ~1.00 GPa and total elongation of only ~7 % at room temperature.

While some HEAs possess both high strength and good ductility, many FCC structured MPEAs (especially solid-solution ones) suffer from poor strength [8]. One approach to enhancing the strength of these alloys is through grain refinement, which can be achieved using thermomechanical processing such as hot rolling. Many studies employ cold rolling as a step during processing of MPEAs, but little systematic work has been performed to study the microstructural and property evolution during hot rolling especially in ductile MPEAs. Mechanical rolling has been shown to refine the microstructure and increase strength [9], [10]. The refined microstructures have also been linked to improved corrosion resistance [11].

In larger scale such as industrial manufacturing of alloys via melting and casting, inclusions are almost unavoidable. Laboratory production of alloys including MPEAs

typically also results in inclusions in the alloys, although very few studies have addressed these inclusions or combated the formation or reduction of these inclusion particles. Inclusions have been observed in laboratory-produced Fe-Ni-Mn-Cr MPEAs [12]], although they were not specifically called out. Inclusions have been known to be the cause of failure in produced alloys. Thus, efforts are typically made to remove or reduce inclusions during industrial production of alloys. Rolling has been shown to change inclusion morphology and even allow the particle's elemental components to dissolve into the matrix [13].

The objectives of this study are to develop a strong and ductile FCC structured Co-free solid-solution MPEAs, as well as to provide insight into the effect of hot rolling on the microstructural evolution (including the grain structure evolution and the changes in inclusions) of a Co-free $Fe_{30}Ni_{30}Mn_{30}Cr_{10}$ MPEA. This particular MPEA was designed based on the Cantor alloy system with the removal of Co and the reduction of Cr content. The reduction of Cr content was motivated by two considerations: 1) to enhance the trend to form an FCC structure, which is beneficial to maintain an FCC matrix even after adding some precipitate-forming elements ($Fe_{30}Ni_{30}Mn_{30}Cr_{10}$ will be used as the matrix for precipitate-hardened MPEAs, which will be reported in separate publications); 2) to improve the corrosion resistance of the MPEA to molten salt, which will be reported in the future.

2. EXPERIMENTAL

The $Fe_{30}Ni_{30}Mn_{30}Cr_{10}$ studied was produced using pure metals (purity >99.9 %) in a vacuum induction furnace, which was pumped down and backfilled with high purity argon three times to ensure a low oxygen content. The furnace was then held at a slightly positive pressure to ensure no air/oxygen could penetrate seals over the duration of the melting procedure. The melt procedure slowly ramped up the furnace to ensure no damage to coils and casting was carried out into a sand mold once all material was liquified. Homogenization was carried out on the cast for 12 hrs at 1100 °C in a muffle furnace. After the homogenization and subsequent cooling, the oxide layer on all sides were removed by machining.

The bulk homogenized sample was heated in a muffle furnace to 1100 °C. Hot rolling was then performed on the sample, with re-heating occurring after the sample temperature dropped below ~950 °C identified by the color of the hot metal. Reductions in thickness were made in 0.1 mm increments with three reductions per heating cycle. The sample was then transferred back to the furnace until it reached the temperature of 1100 °C again. Once the material had reached a desired thickness corresponding to a specific percent reduction, samples were cut off from the bulk material being rolled using an angle grinder while remaining within the temperature margin. Cut off sections were promptly quenched in water to room temperature while the bulk material was returned to the furnace for re-heating. After cut off, no further heat treatment was performed.

Tensile samples were cut using electrical discharge machining with a brass wire. Due to the limited sizes of sections of rolled material, mini-tensile sample dimensions

were chosen with a gauge length of 3 mm and a gauge section of 1 × 1 mm. Tensile tests were performed using a setup optimized for mini-tensile samples and run with a strain gauge. Tensile samples from the 97 % rolling reduction were not able to be produced due to the samples curling up on themselves during cutting by EDM. Initial displacement rate was 0.005 mm/sec and after the strain gauge was removed increased to 0.02 mm/sec. The load frame used was an Instron 6800 tabletop load frame with a 5 kN loadcell attached to it. Hardness measurements on all samples was performed using a Struers Duramin 5 Vickers hardness tester. Electron backscatter diffraction (EBSD) was performed at 30 kV with a working distance of 5 mm for the objective lens and a working distance of 2.2 mm for the charge-coupled device camera. Electron dispersive spectroscopy (EDS) and focused ion beam (FIB) were also used. The controller software for EDS and EBSD was AZtecHKL from Oxford. For FIB, a gallium beam was used to cut into the high Mn particle. This sectioning was performed on a surface level particle of a fracture surface from the as-homogenized sample. All these techniques were performed using a Helios NanoLab 600 FIB scanning electron microscope (SEM).

A strengthening analysis was performed to determine the strengthening contributions from grain refinement as well as dislocation buildup. Grain size effect on strength (i.e., grain boundary strengthening) was analyzed using the Hall-Petch equation. X-ray diffraction (XRD) was carried out to estimate the dislocation density using peak broadening through the Williamson-Hall method. XRD was performed using a Philips MRD XRD ranging from 20 to 120° for 30 min.

3. RESULTS

3.1. AS-CAST AND HOMOGENIZED MICROSTRUCTURES

Fig. 1 shows the dendritic microstructure in the as-cast sample. Dendrites contain higher contents of Fe and Cr, and Mn and Ni segregation to the inter-dendritic regions can be observed. Dendrites are approximately 20–35 μm in width. In addition, Mn-rich particles are found in the as-cast sample. Work by Chen L. indicated that such particles were also present in powder metallurgy samples suggesting that they were not un-melted particles [14]. After homogenization, elements were homogeneously distributed, though some segregation to the grain boundaries can be observed in the Mn map, as revealed in Fig. 2. The oxygen map was added in this case to show the Mn particles that will be discussed later. These particles can also be observed in the BSE image in Fig. 2. The locations of the particles tend to appear as voids as the particles fall out of the matrix during sample preparation. This is most likely due to a significant mismatch of coefficient of thermal expansion between the particle and the matrix resulting in a loss of adhesion during sample cooling. Generally, these particles are in the range of 10–30 μm.

3.2. MICROSTRUCTURE EVOLUTION DURING HOT ROLLING

The changes in microstructure due to hot rolling can be seen in Fig. 3. Fig. 3A–D display EBSD strain maps at 30 %, 60 %, 75 %, and 97 % reduction, respectively. Grain refinement is evident throughout the different rolling reductions. Greater reduction also results in internal strain inside grain interiors rather than just strain at the grain boundaries.

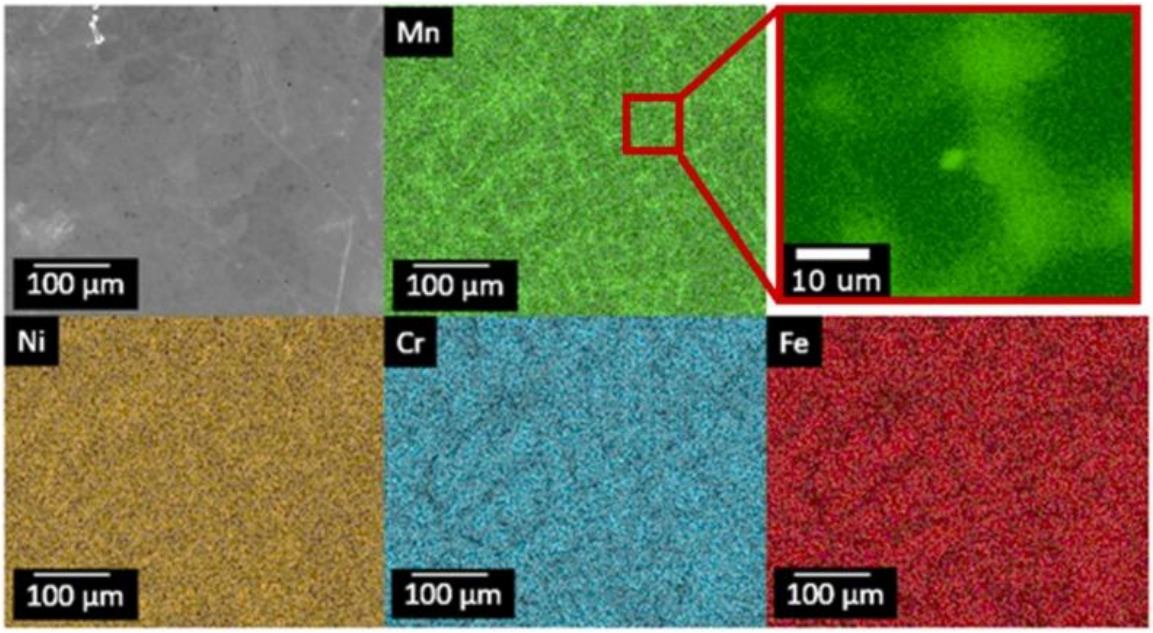

Figure. 1. SEM image and EDS elemental maps showing the as-cast microstructure: dendritic microstructure can be seen with Fe- and Cr-rich dendrites and Mn- and Ni-rich inter-dendritic areas. Mn-rich inclusion particles are small dark spots in the SEM image.

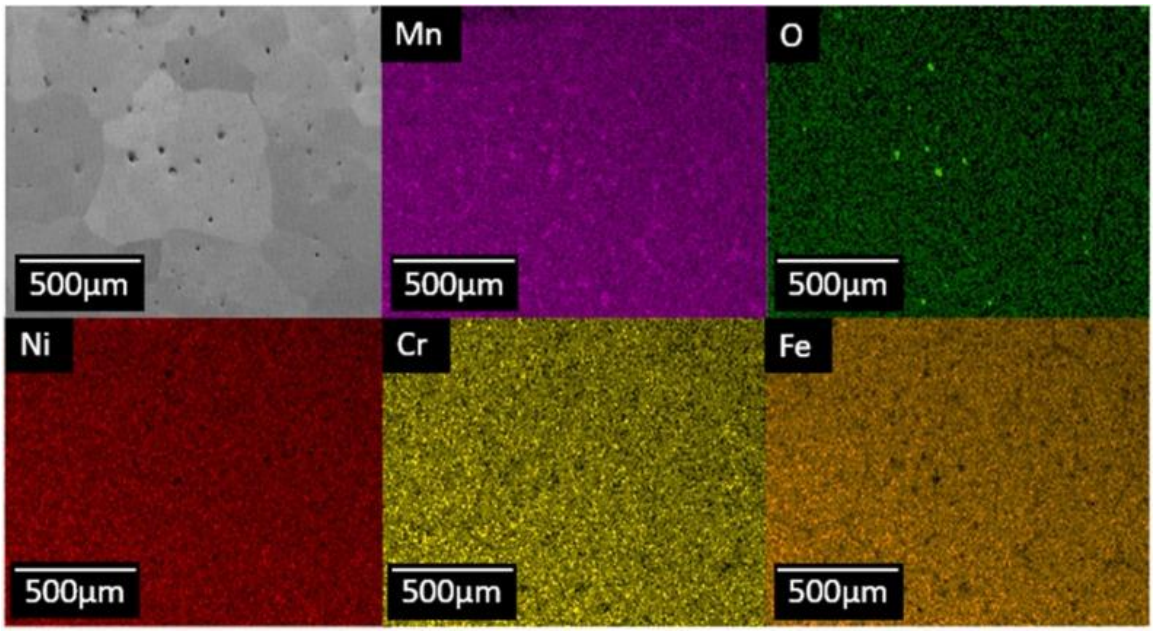

Figure. 2. SEM image and EDS elemental maps showing homogenized microstructure after 12 hr at 1100 °C: dendritic microstructure is removed; Some Mn-rich particles are visible in the Oxygen map due to Mn oxidizing after polishing.

The internal strain also can be linked to future new grain formation due to recrystallization during heating cycles. In Fig. 3a large unresolved/unindexed areas correspond to voids, which may be due to casting defects or owing to the falling of Mn particles during sample preparation. Due to the forging happening during hot rolling, casting defects between are closed and welded shut between Fig. 3a and 3b. At lower reductions, the recrystallization is already evident. At 60 % reduction, seen in Fig. 3b, the strain inside the grains is very low; at 75 % reduction, grain internal strain begins to build up. Grain refinement does not proceed homogenously. Instead, refinement occurs initially near prior grain boundaries, which exhibit a high degree of local deformation and accordingly a higher driving force for recrystallization. Even at 60 % reduction, although the grain refinement is more extensive, large grains still exist, with only small amounts of dislocations inside the grains. At 75 % reduction, the grain shape becomes much more equiaxed. At 97 % reduction in Fig. 3d a microstructure can be seen which has evident internal strain and no large grains can be observed.

3.3. EFFECTS OF ROLLING ON MECHANICAL PROPERTIES

Tensile test results displayed in Fig. 4 show the effect of rolling on the tensile properties of the Fe30Ni30Mn30Cr10 MPEA. Strength increases of 60 MPa for YS and an increase in UTS of 62 MPa can be observed between the 30 % and 60 % hot rolled samples. Ductility increased in this time due to the reduction of casting porosity. The bimodal grain size distribution also allows the large grains to handle more deformation [15].

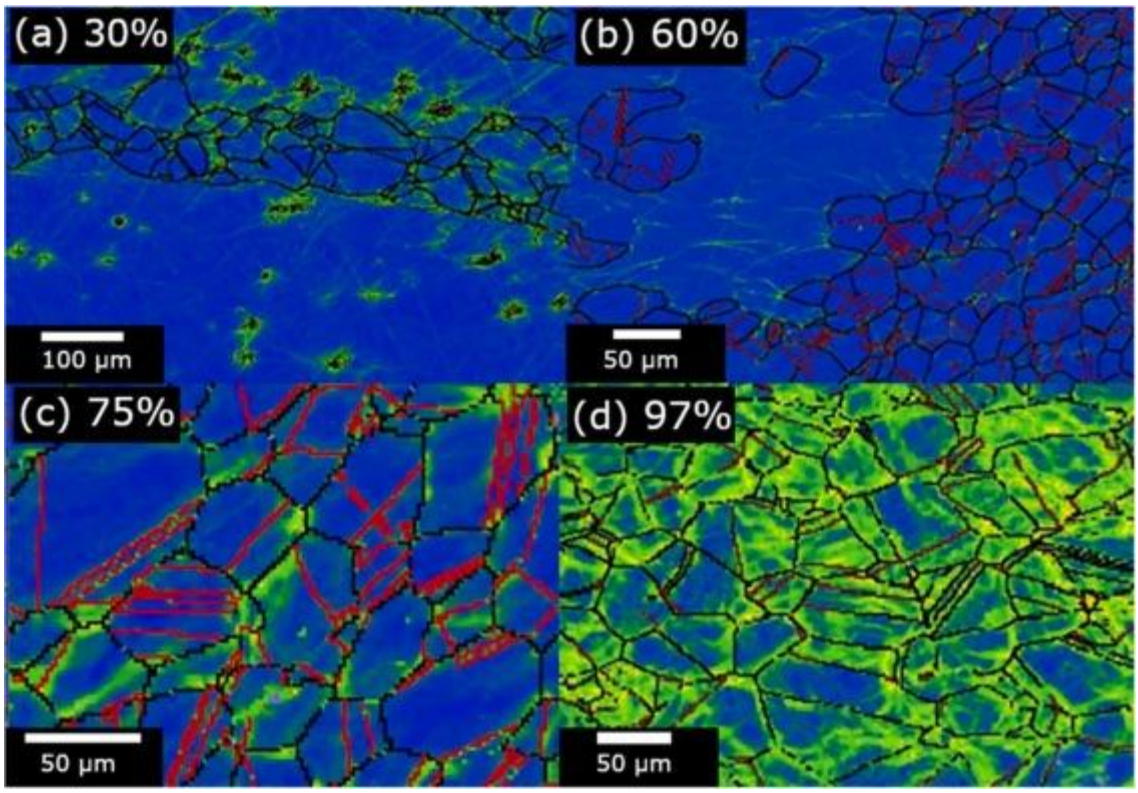

Figure. 3. EBSD strain map showing the microstructure evolution during rolling: (a) 30 % reduction, (b) 60 % reduction, and (c) 75% reduction. Grain sizes vary, with extremely large grains present at reductions of 30 % and 60 %. Noticeable internal strain buildup is only seen at high reduction percentages. A scale of Blue to yellow was used to show strain buildup though this strain is not absolute but relative to surrounding crystal misorienation. Red grain boundaries are twin boundaries with a range of 60 ± 3°. All other grain boundaries 15° + are shown in black. Low angle grain boundaries are not denoted in this figure.

Typical Hall-Petch relation (effect of grain size on strength with smaller grain sizes resulting in higher strength) is observed with subsequent samples reducing in ductility but increasing strength. The only sample to break this trend is no reduction sample to 30 % reduction where casting defects have been closed. The 75 % reduction sample exhibits a yield strength of 595 MPa, a UTS of 710 MPa, a uniform elongation of 25 %, and an elongation-to-failure of 40 %. This sample is strong and ductile, for FCC structured solid-solution MPEAs.

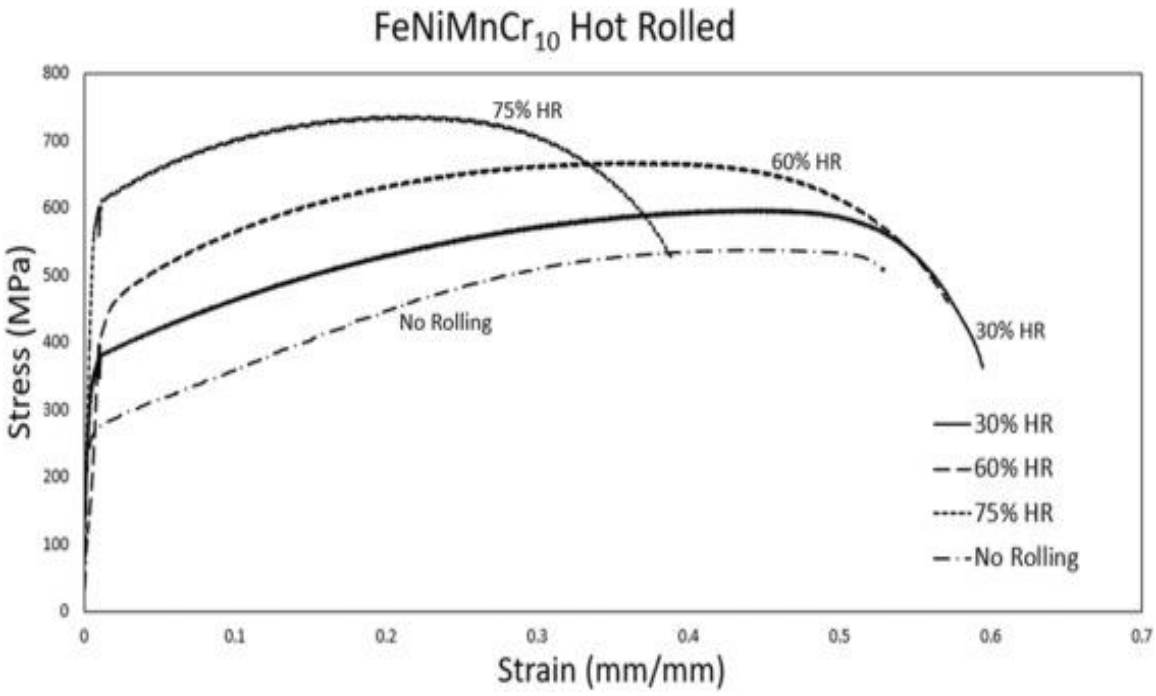

Figure. 4. Engineering stress-strain curves from tensile tests at different rolling reductions. Pre-rolling sample has a YS of 265 MPa and a UTS of 507 MPa at a ductility of 54 % while at 75 % reduction YS is 605 MPa and UTS is 710 MPa at 40 % ductility. While 97 % rolling reduction EBSD data are shown in Fig. 3, due to the small thickness (~1.2 mm) and internal strain in the sample, tensile samples were not able to be produced.

3.4. INCLUSION PARTICLE COMPOSITION

The black spots in the SEM image in Fig. 2, as previously stated, correspond to voids left by particles that fell out during the polishing process. In Fig. 5a particle can be observed on a fracture surface from the homogenized sample. This particle was sectioned using a focused ion beam to determine the particle's internal chemistry without exposure to air. Table 1 shows the composition at different positions as measured by EDS. The results indicate that the particle is almost pure Mn. In addition, this particle has an attached tail much like a MnS inclusion in steels, but this is an exception and almost all

particles have only the round body without a tail. This particle was chosen to show that even particles with tails are effectively pure Mn.

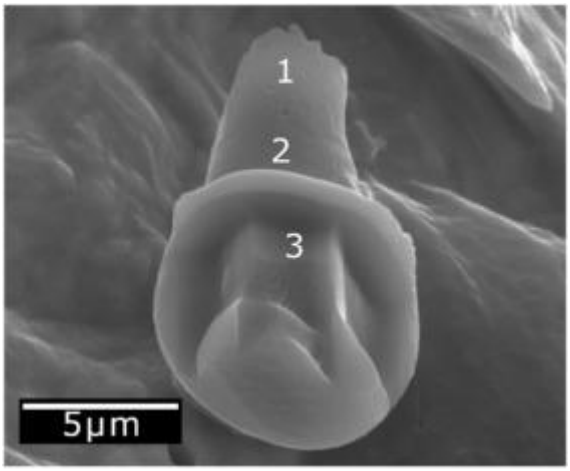

Figure. 5. SEM image of a Mn-rich particle on a fracture surface of the as homogenized tensile sample, which has been cut open using a focused ion beam to perform EDS to obtain the internal chemistry without any contamination by the outside atmosphere. The particle shown has the addition of a tail, but this is not common, and most particles are spherical without tails.

Table 1. Elemental composition of the Mn-rich particle at different locations of the particle (see Fig. 5), measured by EDS point scans. (*) Oxygen has been artificially added here to showcase that these particles are not MnO for positions 3 and the shell. These results indicate that the particle itself is effectively pure Mn. Shell is used for area 3 before the surface had been removed. Positions 1 and 2 are part of a Mn sulfide tail which while showcased in this figure is not common on most particles.

Position / **Elements**	**1 (wt %)**	**2 (wt %)**	**3 (wt %)**	**Shell (wt %)**
O*	35.2	1.3		
Mn	29	55.9	97	95.11
S		39.1		
Fe	16.1	1.5		1.75
Ni	14.2	1.4	1.1	1.43
Cr	5.5	0.8	1.9	1.71

3.5. EFFECT OF HOT ROLLING ON Mn-RICH PARTICLES

Rolling was also used as a technique for reducing both the size and volume/area fraction of the Mn-rich particles. Fig. 6 demonstrate changes to Mn-rich particles with increased hot rolling reduction. The particle morphology has also been changed to be slightly stretched in the direction of rolling. This phenomenon of particle distortion only occurs at higher rolling percentages.

During rolling the Mn-rich particles were deformed and became elongated along the rolling direction. This phenomenon can be seen in Fig. 7. Fig. 7a and 7b shows a particle that has been deformed and elongated; the EDS map confirms that this is a Mn-rich particle. Another particle is displayed in Fig. 7c. The shape of the particle is from bottom left to top right, in line with the rolling direction. A majority of the particles have

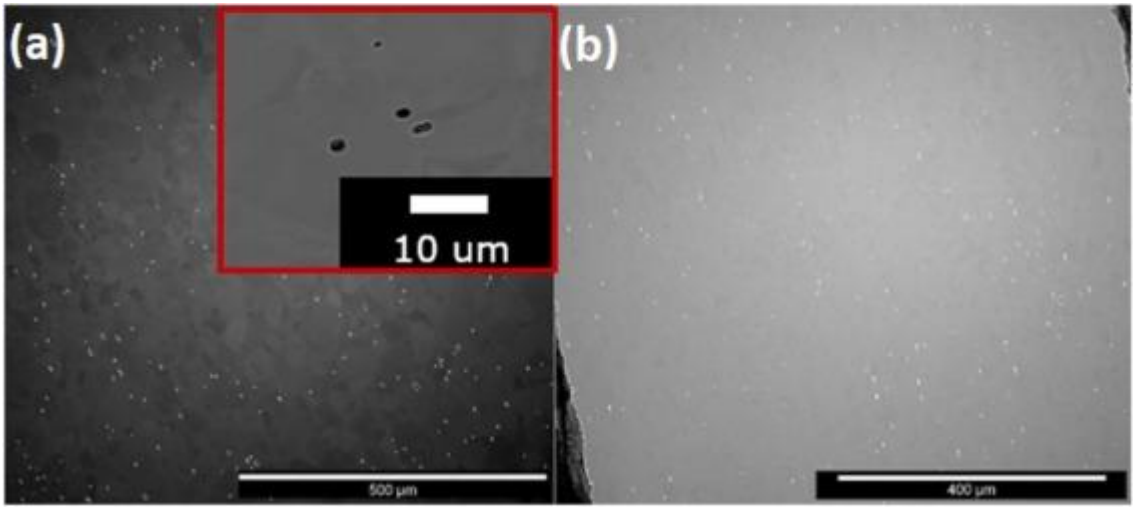

Figure. 6. SEM images showing distribution of Mn-rich particles in the hot rolled $Fe_{30}Ni_{30}Mn_{30}Cr_{10}$ MPEA: (a) 75 % rolling reduction the cutout in (a) shows the morphology of the particles; (b) 97 % rolling reduction. The particles exhibit white/bright borders. Qualitatively the number of particles is reduced with an increase in the rolling reduction.

fallen out of the matrix during the polishing procedure, leaving an empty space on the surface.

From the EDS maps, this particle seems to be almost pure Mn, and small parts of it remain attached to the matrix on the surface. It is likely that before polishing the particle had already been broken into pieces, and some pieces with weak bonding to the matrix easily fell off during polishing, whereas other pieces more strongly adhered to the matrix remained attached to the surface after polishing. It is surmised that these smaller particle parts may be re-dissolved into the matrix or may become too small to be detected by SEM.

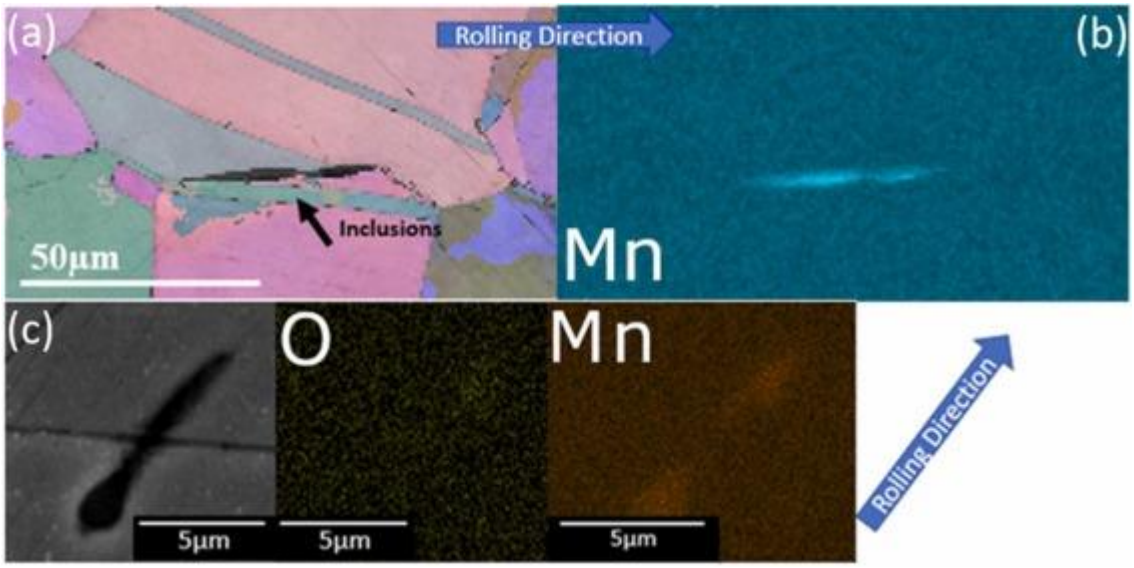

Figure. 7. SEM data showing Mn-rich inclusion particles in 99.5 % rolling reduction sample: (a) EBSD orientation map of an inclusion particle that has been deformed by rolling; (b). EDS map corresponding to (a) showing the Mn particle; (c) another particle deformed/elongated along the rolling direction, where the first sub-image is an SEM image, followed by O and Mn EDS maps.

3.6. MICROSTRUCTURAL SOURCES FOR STRENGTHENING

Sources for the strengthening in the hot rolled samples can be seen in Table 2. The average grain size initially decreases. Following work by Lehto. P, when calculating the average grain size, values from the 1st and 99th percentile were excluded,

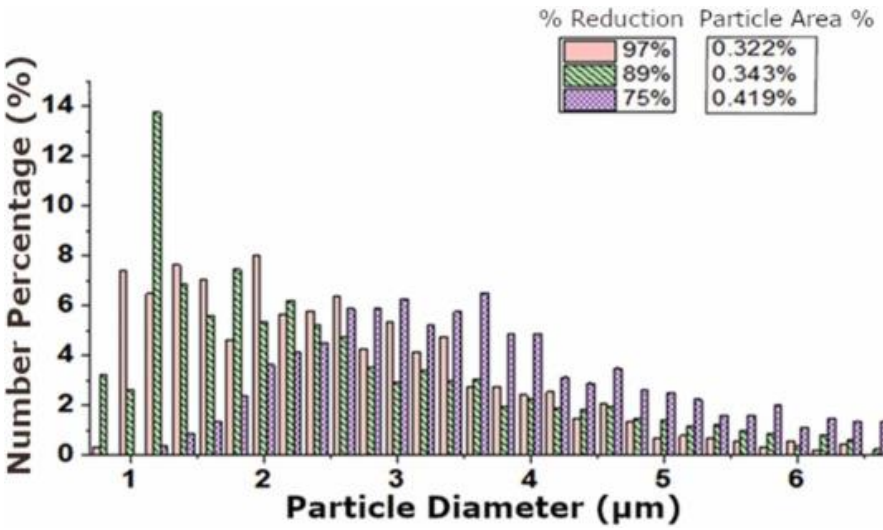

Figure. 8. Number percentage of particles with different diameters, after various hot rolling reduction.

since those grains were either too small or too large, which may askew the average value significantly [16]. After initial grain size reduction (due to dynamic recrystallization), grain size reaches a minimum at 60 % reduction, and then starts to grow again (owing to grain growth at the rolling temperature). Dislocation density was determined using the Williamson Hall plot taken from XRD data of each rolling condition. The slope of each line is the microstrain, ε, and the y-intercept is equal to , where K= 0.9 is a constant, $\lambda = 0.15405$ nm is the Cu Kα wavelength, and D is the crystallite size in nanometers. The dislocation density is then calculated using the equation , where ε is the micro strain, D is

the crystallite size, and b is the Burger's vector, calculated as 0.256 nm. The dislocation density is too low for determination in 30 % and 60 %, resulting in non-real values, but the dislocation density clearly increases from 75 % to 97 % rolling reduction as can be seen in Table 2.

Table 2. Shows the source of strengthening over different rolling reductions. Initial strengthening occurs due to grain size reduction. This changes after 75 % reduction as grain size grows slightly but dislocation buildup results in dislocation strengthening. Initial dislocation density numbers are incorrect due to the extremely low dislocation density leading to negative strain numbers in the Williamson-Hall plot.

Roll Reduction	*30 %*	*60 %*	*75 %*	*97 %*
Williamson-Hall Plot	y = −0.0012x + 0.0039	y = −0.0034x + 9E-05	y = 1.91E-04x + 4.40E-04	y = 1.97E-03x + 4.57E-03
Grain Size diameter (um)	2.34E + 01	1.76E + 01	3.26E + 01	3.20E + 01
Dislocation density (m^−2)	-4.57E + 14	-2.99E + 13	8.20E + 12	8.79E + 13

4. DISCUSSION

4.1. MICROSTRUCTURAL EVOLUTION DUE TO HOT ROLLING OF $FE_{30}NI_{30}MN_{30}CR_{10}$ MPEA

Hot rolling was chosen as a grain refinement technique for this relatively ductile single-phase FCC solid-solution Fe30Ni30Mn30Cr10 MPEA. Initial grain refinement occurred along prior grain boundaries (Fig. 3a) where dislocations accumulated, resulting in recrystallization during deformation. The smaller grains that began to appear at higher

rolling reductions in the hot rolled microstructure are much more equiaxed and little residual strain is left in the grain interior (Fig. 3b), suggesting that the grains experienced recrystallization [17]. The samples also underwent annealing due to being reheated to 1100 °C between rolling passes, and therefore static recrystallization was also possible. However, the increase in the strain inside the grains at high rolling reductions (evident in Fig. 3d) indicated that dynamic recrystallization was dominant since static recrystallization would result in reduced grain internal strain. The buildup of strain at higher reductions (≥ 75%) can be explained due to the reduced thermal mass of the sample resulting in faster cooling as well as a larger reduction in thickness causing more strain per pass.

4.2. ROLLING EFFECT ON MECHANICAL PROPERTIES

In the present study, hot rolling has been shown to increase the strength of the Fe30Ni30Mn30Cr10 MPEA (Fig. 4). This strength enhancement is primarily due to the reduced grain size in the microstructure, which is known as the Hall-Petch relation [18]. Quantification of this relationship though is difficult as the bi-modal grain size distribution does not allow for a single grain size number to be used [19]. Rolling of very ductile materials such as aluminum shows similar behavior to that of $Fe_{30}Ni_{30}Mn_{30}Cr_{10}$ MPEA investigated in this study. Results from [20] showed small grains forming along the former grain boundaries as these are sites for dislocation accumulation and subsequent recrystallization static. In addition to grain refinement, the buildup of strain inside the grains (Fig. 3) at higher rolling reductions (≥ 75%) also improved the strength. However, this is considered a secondary contribution, since the hot rolling was performed

at a high temperature of 1100 °C, and the accumulated dislocation density was anticipated to be low at such a high temperature.

4.3. STRENGTHENING MECHANISMS

A strengthening analysis was performed to determine the strengthening mechanisms from hot rolling. Both the Hall-Petch relationship as well as dislocation strengthening were investigated to determine the main strengthening contributors. Grain size reduction plays a major role in the initial strength increases. The initial millimeter sized grains hamper efforts to determine grain size effect [16]. Excluding these large grains allows an average grain size to be determined reflective of the strength. Grain size reduction stops after 60 % rolling reduction due to the dynamic recrystallization occurring during hot rolling being balanced out by grain growth. Due to the increased pressure during higher rolling reduction and reduced time to reach rolling temperature again, dislocation buildup occurs at higher rolling reductions, making dislocation strengthening the main strengthening contributor.

4.4. HOT ROLLING EFFECT ON MN-RICH PARTICLES

Hot rolling was investigated as a process to reduce Mn-rich particles in the Fe30Ni30Mn30Cr10 MPEA. In steels, similar processes have shown promise in changing the morphology and count of MnS inclusions [21]. In steels, Mn-rich particles are often MnS or MnO. However, in this Fe30Ni30Mn30Cr10 MPEA, it is thought that these Mn-rich particles are pure Mn and they form during cooling – they precipitate out of a solid solution super saturated in Mn [22]. Such particles have also been observed in additively manufactured material as well, further supporting that these particles are precipitated out

of a super saturated solution. Additionally, additively manufactured materials also show that these are not un-melted particles, rather they form during cooling after melting [14]. It is important to try to reduce such inclusion particles, as they have been shown to be the site for crack initiations and accordingly lead to failure in steel parts [23]. Similarly, it is beneficial to reduce inclusion particles in MPEAs, although such a topic has not really been studied previously. Results in Fig.7, Fig. 8 clearly indicated that the diameter and area percentage of Mn-rich particles in the $Fe_{30}Ni_{30}Mn_{30}Cr_{10}$ MPEA were reduced. The exact mechanisms for the reduction in particle diameter and area percentage are unknown, but it is conjectured that multiple factors play roles. Firstly, in order to accommodate the plastic deformation as a whole during hot rolling, strain accumulates near the particles, leading to large local strain. Secondly, the particles are fractured, especially at high strain (high rolling reductions), and thus reduced in size. Finally, locally the particles, especially the small parts, are slowly dissolved into the matrix due to the increased strain present in the matrix allowing for extended solubility or supersaturation of Mn in the matrix [24].

5. SUMMARY AND CONCLUSIONS

A Co-free Fe30Ni30Mn30Cr10 MPEA, which is significant for applications requiring avoidance of Co, was developed, and fabricated via casting, homogenization, and hot rolling at 1100 °C. Tensile testing was performed on the alloy hot rolled to different reductions. Microstructure characterization was carried out, via SEM, EDS and EBSD. The main findings of this study are:

1. Hot rolling remarkably improved tensile properties of the alloy. The tensile strength increased with the increase of rolling reduction. When rolling reduction increased from 30 % to 60 %, yield strength increased from 390 to 450 MPa, and UTS increased from 590 to 650 MPa, while the ductility almost remained at ~60 %, which was owing to the bimodal grain size distribution in the hot rolled samples up to 60 % rolling reduction. At rolling reductions, the grain structure became equiaxed, and the grain size distribution was much narrower. The sample with 75 % rolling reduction achieved a yield strength of 595 MPa, an UTS of 710 MPa, and a ductility of 40 %, representing a strong and ductile FCC structured solid-solution MPEA.

2. Hot rolling is an effective way to reduce the size and area fraction of Mn-rich particles, commonly seen in Mn-containing steels and MPEAs (even though largely neglected in previous studies on MPEAs). Mn-rich particles were deformed along the rolling direction, and fractured into smaller parts, which may be dissolved into the matrix at high rolling reductions.

REFERENCES

[1] D.B. Miracle, O.N. Senkov, A critical review of high entropy alloys and related concepts, Acta Mater. (2017). https://doi.org/10.1016/j.actamat.2016.08.081.

[2] K.Y. Tsai, M.H. Tsai, J.W. Yeh, Sluggish diffusion in Co-Cr-Fe-Mn-Ni high-entropy alloys, Acta Mater. (2013). https://doi.org/10.1016/j.actamat.2013.04.058.

[3] T. Shi, P.H. Lei, X. Yan, J. Li, Y. Di Zhou, Y.P. Wang, Z.X. Su, Y.K. Dou, X.F. He, D. Yun, W. Yang, C.Y. Lu, Current development of body-centered cubic high-entropy alloys for nuclear applications, Tungsten. 3 (2021) 197–217. https://doi.org/10.1007/s42864-021-00086-6.

[4] Y. Shi, B. Yang, P.K. Liaw, Corrosion-resistant high-entropy alloys: A review, Metals (Basel). 7 (2017) 1–18. https://doi.org/10.3390/met7020043.

[5] Z. Wu, H. Bei, Microstructures and mechanical properties of compositionally complex Co-free FeNiMnCr18 FCC solid solution alloy, Mater. Sci. Eng. A. 640 (2015) 217–224. https://doi.org/10.1016/j.msea.2015.05.097.

[6] N.A.P.K. Kumar, C. Li, K.J. Leonard, H. Bei, S.J. Zinkle, Microstructural stability and mechanical behavior of FeNiMnCr high entropy alloy under ion irradiation, Acta Mater. 113 (2016) 230–244. https://doi.org/10.1016/j.actamat.2016.05.007.

[7] B.B. Bian, N. Guo, H.J. Yang, R.P. Guo, L. Yang, Y.C. Wu, J.W. Qiao, A novel cobalt-free FeMnCrNi medium-entropy alloy with exceptional yield strength and ductility at cryogenic temperature, J. Alloys Compd. 827 (2020) 1–7. https://doi.org/10.1016/j.jallcom.2020.153981.

[8] Z. Li, S. Zhao, R.O. Ritchie, M.A. Meyers, Mechanical properties of high-entropy alloys with emphasis on face-centered cubic alloys, Prog. Mater. Sci. 102 (2019) 296–345. https://doi.org/10.1016/j.pmatsci.2018.12.003.

[9] C.W. Tsai, Y.L. Chen, M.H. Tsai, J.W. Yeh, T.T. Shun, S.K. Chen, Deformation and annealing behaviors of high-entropy alloy Al0.5CoCrCuFeNi, J. Alloys Compd. (2009). https://doi.org/10.1016/j.jallcom.2009.06.182.

[10] B. Bay, N. Hansen, D. Kuhlmann-Wilsdorf, Microstructural evolution in rolled aluminium, Mater. Sci. Eng. A. (1992). https://doi.org/10.1016/0921-5093(92)90002-I.

[11] K.D. Ralston, D. Fabijanic, N. Birbilis, Effect of grain size on corrosion of high purity aluminium, in: Electrochim. Acta, 2011. https://doi.org/10.1016/j.electacta.2010.09.023.

[12] N.D. Stepanov, D.G. Shaysultanov, M.A. Tikhonovsky, G.A. Salishchev, Tensile properties of the Cr-Fe-Ni-Mn non-equiatomic multicomponent alloys with different Cr contents, Mater. Des. (2015). https://doi.org/10.1016/j.matdes.2015.08.007.

[13] R. Li, M. Yao, W. Liu, X. He, Effects of cold rolling on precipitates in Inconel 718 alloy, J. Mater. Eng. Perform. 11 (2002) 504–508. https://doi.org/10.1361/105994902770343737.

[14] L. Chen, Z. Li, P. Dai, P. Fu, J. Chen, Q. Tang, Effects of carbon addition on microstructure and mechanical properties of Fe50Mn30Co10Cr10high-entropy alloy prepared by powder metallurgy, J. Mater. Res. Technol. 20 (2022) 73–87. https://doi.org/10.1016/j.jmrt.2022.07.067.

[15] M.J.N.V. Prasad, S. Suwas, A.H. Chokshi, Microstructural evolution and mechanical characteristics in nanocrystalline nickel with a bimodal grain-size distribution, Mater. Sci. Eng. A. 503 (2009) 86–91. https://doi.org/10.1016/j.msea.2008.01.099.

[16] P. Lehto, H. Remes, T. Saukkonen, H. Hänninen, J. Romanoff, Influence of grain size distribution on the Hall-Petch relationship of welded structural steel, Mater. Sci. Eng. A. 592 (2014) 28–39. https://doi.org/10.1016/j.msea.2013.10.094.

[17] M.H. Alvi, S. Cheong, H. Weiland, A.D. Rollett, Recrystallization and texture development in hot rolled 1050 aluminum, Mater. Sci. Forum. 467–470 (2004) 357–362. https://doi.org/10.4028/www.scientific.net/msf.467-470.357.

[18] R.W. Armstrong, The influence of polycrystal grain size on several mechanical properties of materials, Metall. Mater. Trans. 1 (1970) 1169–1176. https://doi.org/10.1007/BF02900227.

[19] N. Hansen, Hall-petch relation and boundary strengthening, Scr. Mater. 51 (2004) 801–806. https://doi.org/10.1016/j.scriptamat.2004.06.002.

[20] J.J. Sidor, R.H. Petrov, L.A.I. Kestens, Microstructural and texture changes in severely deformed aluminum alloys, Mater. Charact. (2011). https://doi.org/10.1016/j.matchar.2010.12.004.

[21] K.I. Yamamoto, H. Yamamura, Y. Suwa, Behavior of non-metallic inclusions in steel during hot deformation and the effects of deformed inclusions on local ductility, ISIJ Int. 51 (2011) 1987–1994. https://doi.org/10.2355/isijinternational.51.1987.

[22] Y. Tanaka, F. Pahlevani, S.C. Moon, R. Dippenaar, V. Sahajwalla, In situ characterisation of MnS precipitation in high carbon steel, Sci. Rep. 9 (2019) 1–12. https://doi.org/10.1038/s41598-019-46450-y.

[23] G. Le Roy, J.D. Embury, G. Edwards, M.F. Ashby, A model of ductile fracture based on the nucleation and growth of voids, Acta Metall. 29 (1981) 1509–1522. https://doi.org/10.1016/0001-6160(81)90185-1.

[24] S. Sheibani, S. Heshmati-Manesh, A. Ataie, Structural investigation on nano-crystalline Cu-Cr supersaturated solid solution prepared by mechanical alloying, J. Alloys Compd. 495 (2010) 59–62. https://doi.org/10.1016/j.jallcom.2010.02.034

II. HIGH STRENGTH AND HIGH DUCTILITY SIMULTANEOUSLY ACHIEVED BY TAILORING TI/AL ADDITIONS IN $(FE_{0.3}NI_{0.3}MN_{0.2}CR_{0.2})_{100-X-Y}TI_XAL_Y$ HIGH-ENTROPY ALLOYS

Hans Pommerenke1, Matthew Luebbe1, Jiaqi Duan2, Viraj Ashok1, Ronald O'Malley1, Haiming Wen1*

1 Department of Materials Science and Engineering, Missouri University of Science and Technology, Rolla, MO 65409, USA

2 Warwick Manufacturing Group, University of Warwick, Coventry, CV4 7AL, UK

*Corresponding author: wenha@mst.edu (H.M. Wen).

ABSTRACT

In this study we explored the precipitation strengthened alloy system based on the Fe30Ni30Mn20Cr20 with two different ratios of Al and Ti, i.e., Ti2Al1 and Ti1Al3. Ageing led to an increase in tensile strength in both alloys, however the increase is more significant in Ti1Al3; meanwhile, Ti2Al1 showed a reduced ductility while the ductility of Al3Al remained after ageing. The Ti1Al3 aged system showed an excellent combination of strength and ductility with an ultimate tensile strength (UTS) of 882 MPa and a total elongation of 43%. Both systems exhibited L12 precipitates, though the Ti1Al3 system produced precipitates with an average diameter of 18 nm while the Ti2Al1 system showed the precipitation of 100nm wide um long precipitates. These overgrown L12 were linked to reduced ductility as well as strength. The Al3Ti1 system showed significant promise for future studies.

1. INTRODUCTION

The development of high strength, high ductility alloys has been the goal for high entropy alloys since the first initial research came out in 2004.[1],[17] Often also called MPEAs (Multi-Principal Element Alloys), these alloy systems offer the ability to tailor properties of alloys by using the advantageous properties of different principal elements and supplementing these with alloying elements.[1] Though many MPEAs have been designed and tested, face centered cubic (FCC) alloys are found to be high in ductility but do not display high strength overall[18],[19]. Due to the lack of high strength displayed by FCC based MPEAs much research has pivoted to focus on precipitation strengthened alloys.[15, 20, 21] These alloys allow a ductile matrix to quickly be hardened while still maintaining the ductility to create a high strength high ductility alloy.[11,22] In steels this has been achieved through the use of oxide nano-powders. Oxide-dispersal strengthened steels (ODS Steels) combined with the nano-sized particles dispersed throughout the matrix is similar to that of the nano-precipitate y' precipitate which is aimed to be formed in this work. [23,14,24]

Using the well-researched alloy system of the Cantor alloy (CoCrFeMnNi)[17] as a basis, and with the removal of Co due to the targeted use of the nuclear industry Ti and Al were added to this ductile base to precipitate y'.[16] Previous studies by Chen et al. had shown that the Ti and Al ratio significantly affects which precipitates will form resulting in drastically different mechanical properties.[25,26] Luebbe et al. showed that in the Ti4Al8 system a variety of phases are formed including the desired y' along with the brittle phases such as Chi and B2.[27]

In this study the focus was on the effect of differing ratios of Ti and Al on the mechanical properties of the resultant alloy systems. Based on the work of Luebbe et al. , Chen et al. , and others it is expected that a higher concentration of Ti is less likely to form brittle phases such as Chi or B2 which had been observed by Luebbe et al. , Chen et al. , and others.[16, 27] The resulting alloy systems show promise in creating a high strength high ductility alloy system which has a potential wide range of applications.

2. EXPERIMENTAL PROCEDURE

Vacuum induction furance was used to cast ingots weighing 2.5 kg with target compositions of FeNiMn20Cr20 (Ti0), FeNiMn20Cr20 Ti1Al3 (Al3), and FeNiMn20Cr20 Ti2Al1 (Ti2). The charge materials had a purity above 99.5%. All material was added into a 10 lb Al2O3 crucible, placing magnetic materials (Fe and Ni) on top of Mn, Cr, Ti, and Al to ensure all material was melted with minimal adherence to the crucible walls. Molten metal was poured into no-bake sand molds with a steel chill block at the bottom to promote directional solidification.

Samples were then covered in a stainless-steel bag and homogenized in a muffle furnace at 1150 oC for 5 hours. A protective atmosphere of industrial grade argon was used to protect samples from oxidizing with a flowing rate of 0.2L/min. Subsequently, the samples were quenched in water with the bag open. .

Aging temperature and time were refined from our previous study28. Hardness testing samples were aged at both 650 oC and 750 oC for between 30 min to 120 hrs, followed by air cooling. Aging was performed in a tube furnace under industrial grade

flowing argon at 0.2 L/min. Samples were then tested on a Struers Duramin 5 Vickers hardness tester following ASTM E92 using a 5 second load time at 4.94 N for the testing.

Tensile samples were cut from the cast and homogenized block. Due to the size of the cast, approximately 1x4x7 inches, the tensile samples were reduced in size to have a gauge cross section of6.25x6.75mm and a gauge length of 31mm. These tensile samples were tensile tested in the homogenized and the aged conditions on a Landmark MTS test frame with a 250 kN load cell, in accordance with ASTM E8.

Fracture surface analysis samples were cut from the tensile samples ~1mm from the fracture surface. The fracture surfaces were cleaned with compressed air. Scanning electron microscopy (SEM) was then performed.

All SEM work including electron backscatter diffraction (EBSD) and scanning transmission electron microscopy (STEM) were performed on a Helios Nanolab at 30 kV and 11 nano-amps. SEM and EBSD samples were ground and polished, using 0.02 μm colloidal silica for the final polishing stage. Samples for STEM and transmission electron microscopy (TEM) were prepared by dual-jet electropolishing as well as lift outs performed in the dual-beam focused Ion beam (FIB) in the Helios Nanolab. Samples for electropolishing were polished to a maximum of 600 grit SiC abrasive paper and to a thickness of ~ 50 microns. For electro-polishing the solution was 20% perchloric acid mixed with 80% ethanol. TEM and STEM with EDS were performed on a Talos F200X at 200 kV.

3. RESULTS

3.1. INITIAL AS-CAST HOMOGENIZED MICROSTRUCTURE

Samples taken from the homogenized casts were inspected. The porosity for all samples was found to be 2.3%-2.7%. The grain size was around 2mm^2 as determined by SEM. After homogenization of the the crystal structure was found to be a single-phase FCC as determined by EBSD for all systems. The final compositions in the homogenized state can be seen on table 1 showing a slight variance in the Mn of the Al3 system though all other elements are within the desired range.

Table 1. Shows the final composition after casting for both the Al3 and the Ti2 systems. A slight variance in the Mn in the Al3 system can be observed. All other elements are in the desirable range.

	Ti2 (at%)	Al3 (at%)
Al	1.1	3.0
Ti	2.1	1.2
Cr	19.7	20.4
Mn	20.4	16.1
Fe	29.2	30.5
Ni	27.5	28.8

3.2. MICROSTRUCTURAL DEVELOPMENT DURING AGING

Figure 1 shows the EBSD images of the Ti2 and Al3 systems taken after aging at 650C for 24 hours. It can be seen in Figures 1a and 1b that both Ti2 and Al3 samples have single phase structures. The IPF maps shown in Figure 1c show a single grain with some grain internal strain near the grain boundary. In Figure 1d, the Al3 system, an interesting phenomenon can be observed; sub-grain boundaries can be observed within the primary grain.

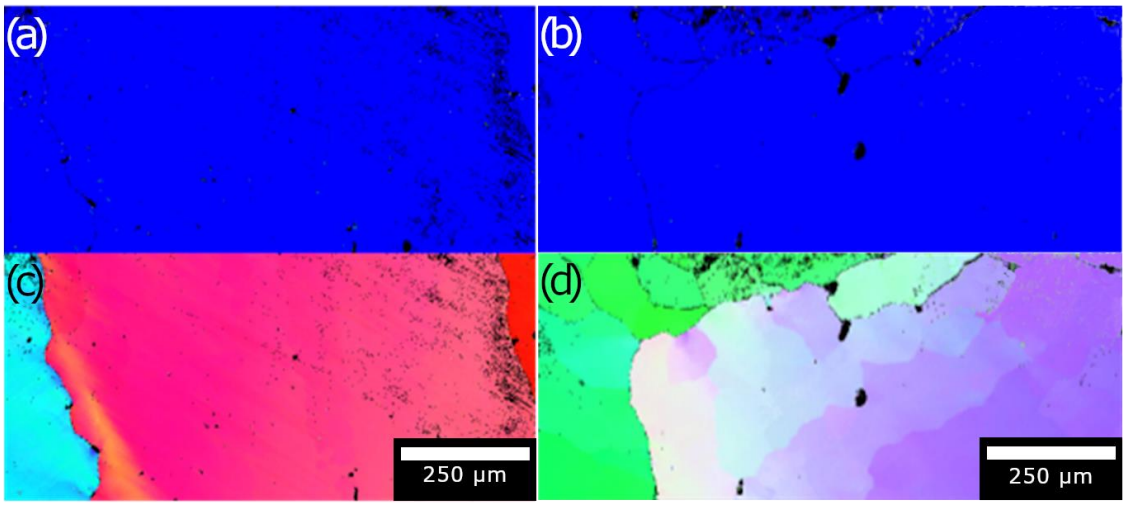

Figure 1. Shows the microstructure of both the Ti2 (a) and Al3 (b) systems aged at 650C for 24 hours. Of note are the lack of any secondary phase visible in (a) and (b) denoted by the blue FCC through microstructural differences in both observable grain size and the existence of sub grains in the Al3 system as can be seen in (d). These sub grains are a result of the fine precipitates pinning dislocations during grain growth. Ti2 (c) and Al3 (d) highlight the orientation and change in orientation in the grains.

STEM and TEM were performed to reveal the microstructure and precipitates, observable in Fig. 2-3. Figure 2(a) shows dark field STEM of the Al3 system after aging for 24 hours at 650C. The outtake in (a) shows a close up of three precipitates. The

precipitates cover an area fraction of 5.35% and the morphology is a elongated oval or rectangle. These precipitates are found in all orientations and are spread throughout grains with no indication of grain boundary preference. Figure 2b shows dark field STEM of Ti2 precipitates post aging at 650C for 24 hours. The precipitates in the Ti2 system are larger than in the Al3 system. Rather than equally distributed, the precipitates behave more like a secondary phase with interconnected networks. Volume fraction was not able

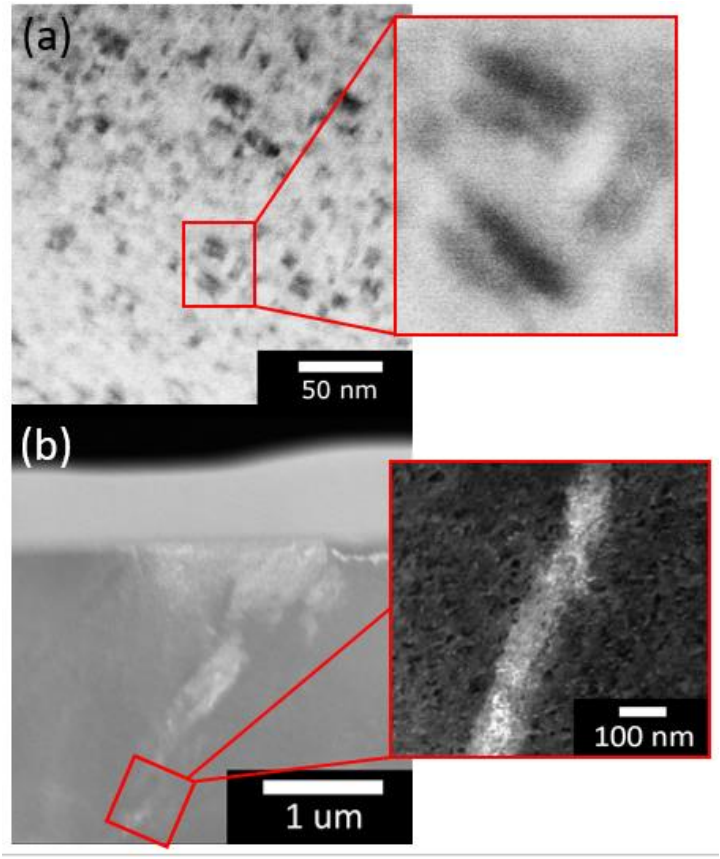

Figure 2. Shows the precipitates of the Al3(a) and Ti2 (b) systems. (a) Shows the precipitates in Al3 showing a dense presence in grains. These principates have an average diameter of 20nm and a volume fraction of 5.35%. (b) shows the precipitates in Ti2 as lighter areas in the image. The volume fraction is hard to determine due to the large size and lack of distribution throughout the grain. The large precipitates act as a secondary phase.

to be determined as only large singular precipitates were found in the lamella though a close area EBSD scan did not reveal the precipitates. Both systems precipitates are theorized to be FCC precipitates as identified by XRD which can be seen in figure 3. The XRD patterns show both an FCC phase as well as a barely visible L_{12} phase showing both systems form L_{12} precipitates though of different size and morphology.

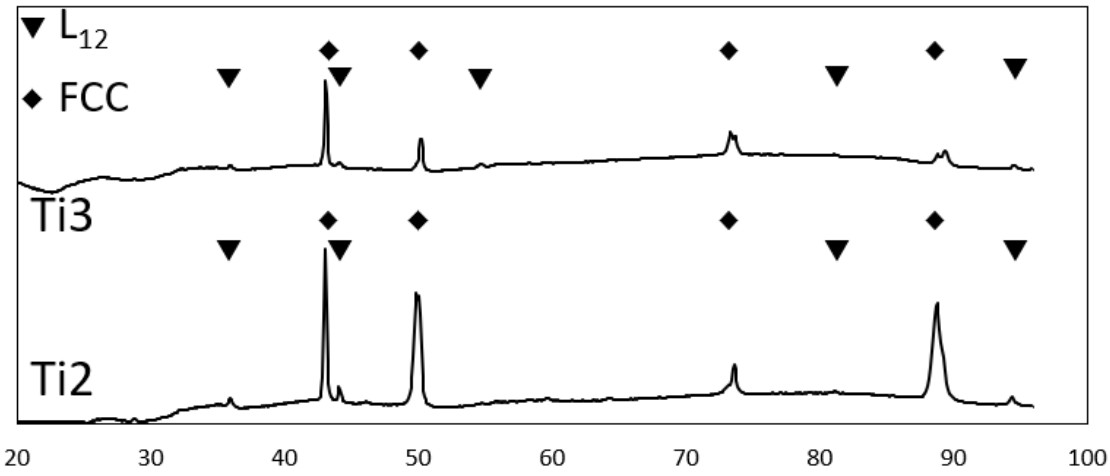

Figure 3. Shows the XRD patterns of each alloy with the L12 and FCC peaks marked.

Figure 5 shows an example of precipitates found in both systems in terms of composition. Pictured is a precipitate from the Ti2 system. This precipitate shows clear Ni enrichment. No Ti enrichment is seen, but most Ni-Ti precipitates allow for Al to replace Ti suggesting little to no enrichment in comparison to the matrix would be visible

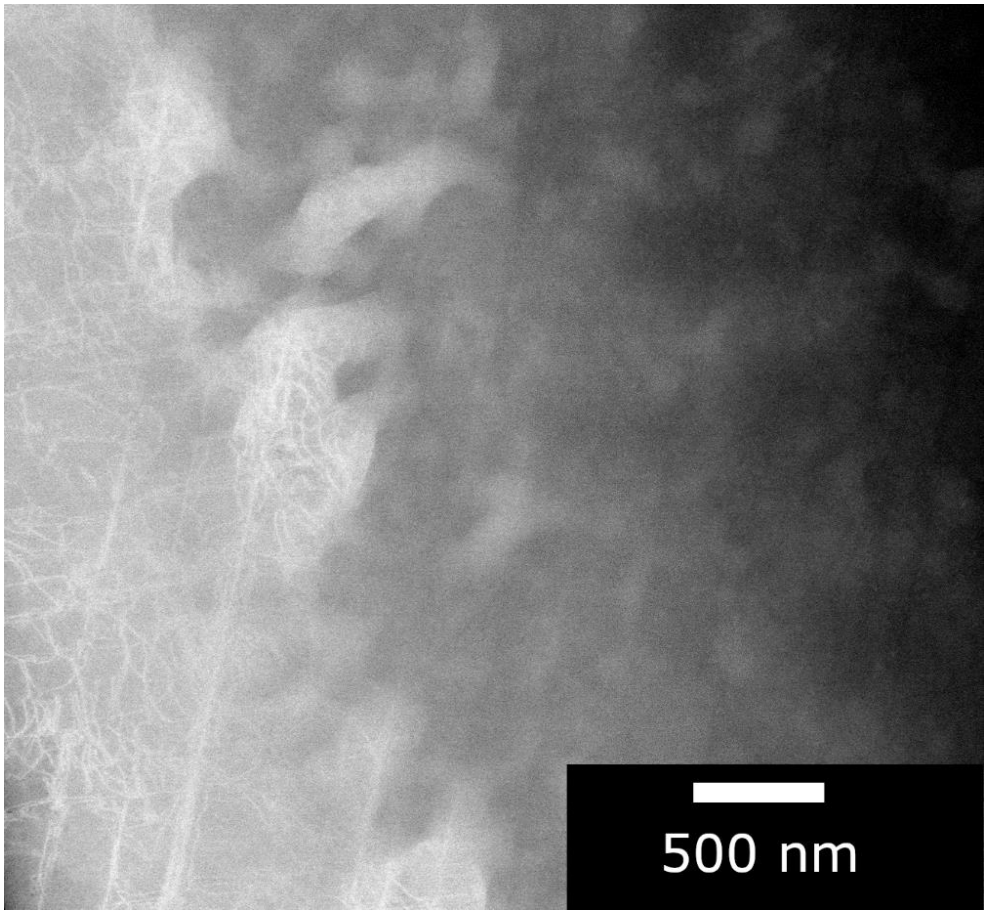

Figure 4. Shows dislocations formed during precipitate formation. This sample shows the Ti2 aged sample with a high amount of dislocations lines on the left side of the image. Al3 system does not exhibit this dislocation buildup.

3.3. MECHANICAL TESTING

Post homogenization hardness for each system remained 135 HV with a slight increase to 145 HV in the Ti2 system. Figure 6 shows the variation in hardness as a function of aging time at both 650 ^{o}C and 750 ^{o}C Figure 6(a) for the Al3 system at 650C shows a steady increase in hardness to 325 HV until 12 hours of aging, followed by a

slow increase to 350 HV after 120 h. The Ti2 at 650 ºC system shows an initial rapid increase to 345 HV in at 1 hour, followed by a slow increase to a hardness of 390 HV at 120 hrs of aging.

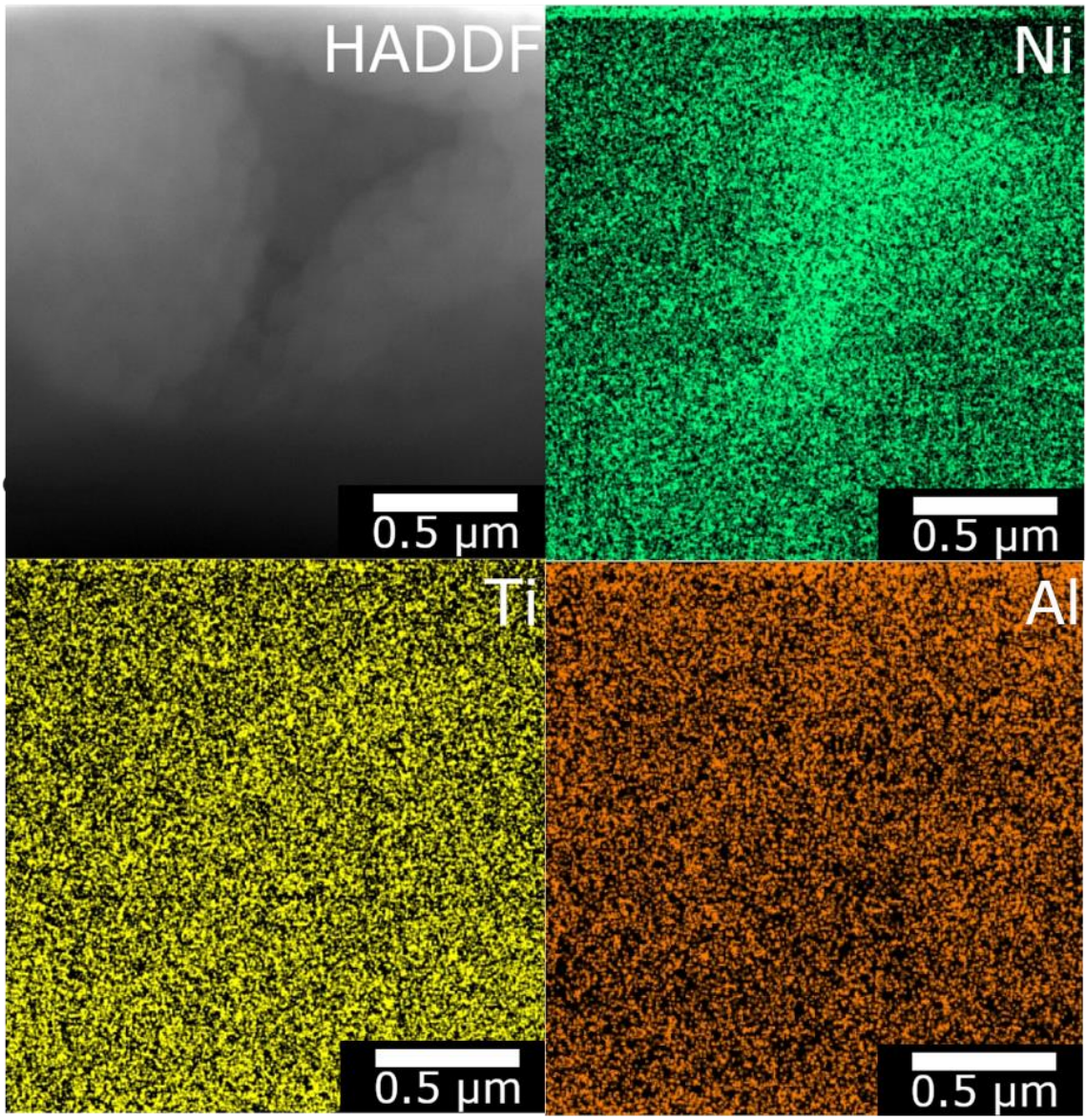

Figure 5. Shows a large precipitate in the Ti2 system. While larger than other precipitates, most precipitates are in the sub 100 nm range with some precipitates growing to the 100s of nm range.

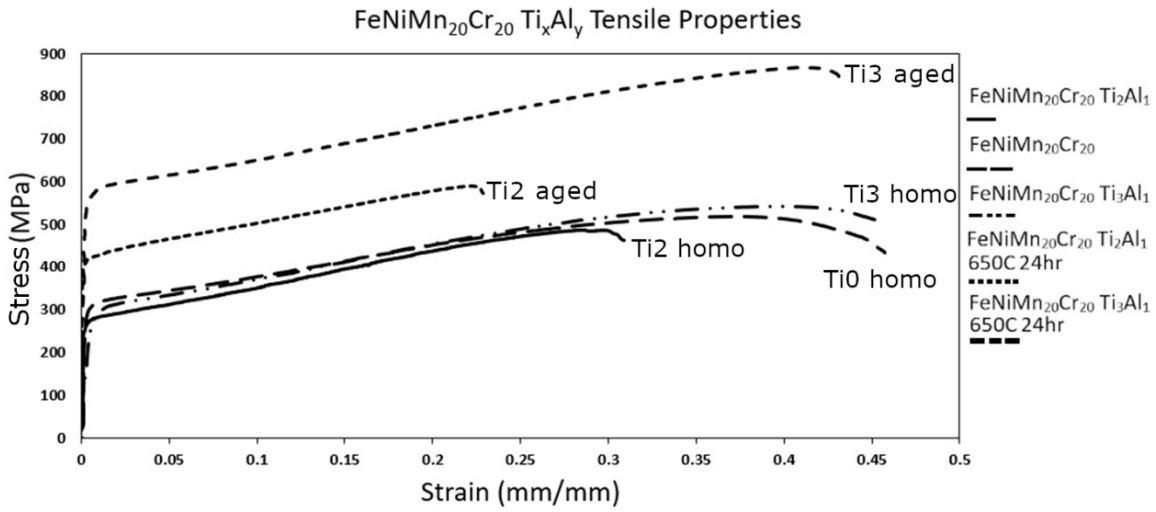

Figure 6. Shows the effect of aging temperature and aging time on the hardness and therefore the precipitate formation in each alloy based on time and temperature. (a) shows the change in hardness at 650C with an initial fast growth followed by a steadier growth over time leveling out at approximately 380 HV for both Ti2 and Al3 systems (b) shows an initial fast growth with a peak hardness achieved after 1 hour aging at and steady state hardness ranging within 50 HV of each other.

In Figure. 6b, the hardness of Ti2 increased to 300Hv after 30 mins of ageing and it plateaued during the subsequent ageing. The hardness of Al3 increased to 320Hv during the first hour of ageing, and its value remained constant thereafter. For Ti2, ageing at 750C yielded a lower hardness compared to 650C. For Al3, the highest hardness value achieved at 750C is comparable to that achieved at 650C but required much shorter aging time.

Tensile testing results are shown in Figure 7. The testing revealed the differences between the different Ti/Al ratios. The Ti0 shows a YS of 270 MPa, a UTS of

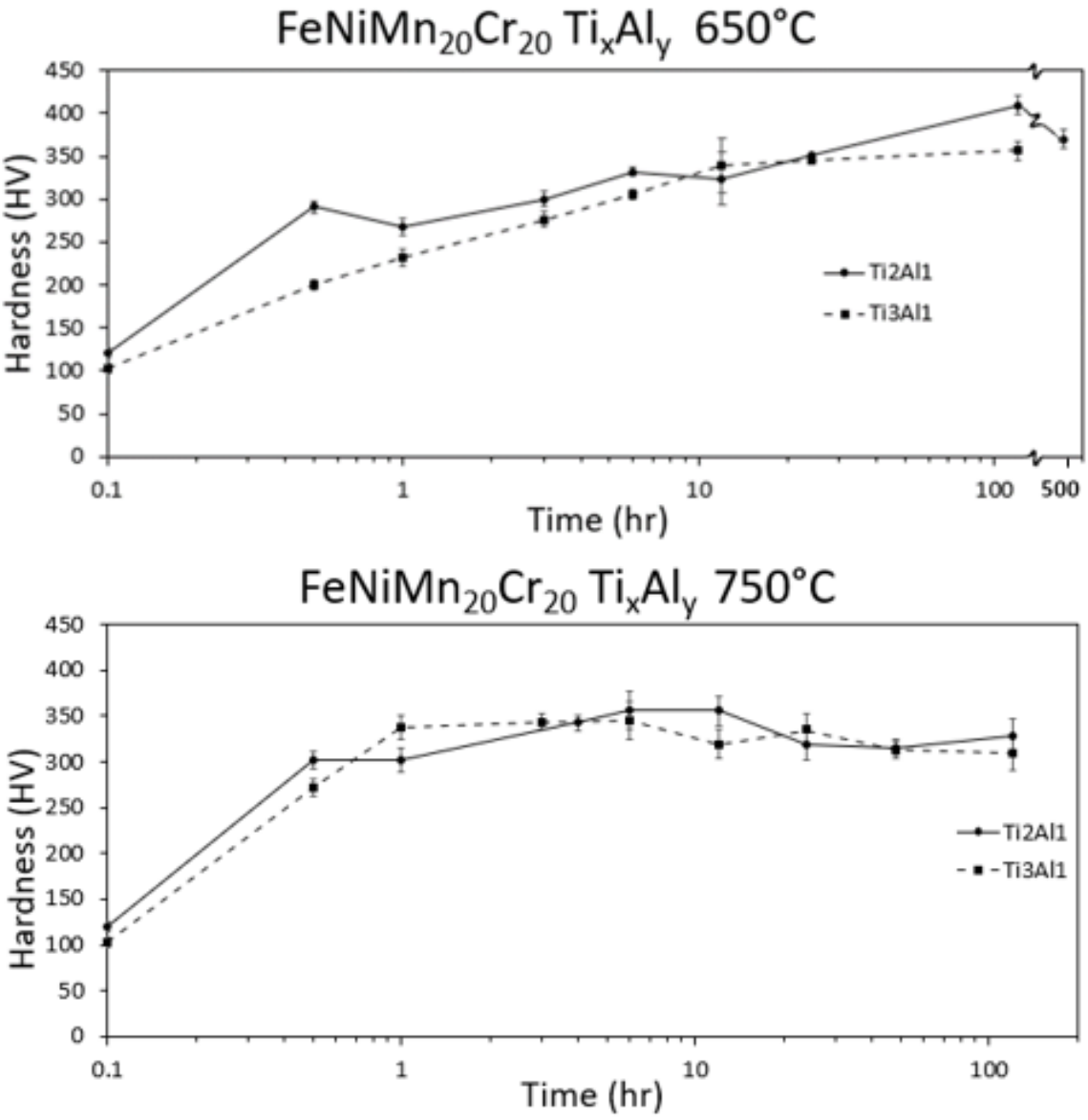

Figure 7. Shows the tensile strength of different alloys, Al3 (540 MPa and 39.6% elongation at UTS) and Ti0 (515 MPa and 38.2% elongation at UTS) show similar strength and elongation. Ti2 has shows a slightly reduced strength at 490 MPa but a significant reduction in elongation at 27.6% at UTS. Aging at 650C for 24 hr shows a large change in Ti2 and Al3. Ti2 has an increase of 100 MPa to 590 MPa at an elongation of 22.4% at UTS. Al3 sees a significant increase in strength up to 882 MPa, an increase of 342 MPa. YS changes from ~300 MPa preaging for Ti0 Ti2 and Al3 to YS of 405 MPa for Ti2 and YS of 585 MPa for Al3.

515 MPa and an elongation of 46.1%. The homogenized Al3 shows a slight increase in UTS at 540 MPa compared to Ti0, while the homogenized Ti2 system, shows a significant drop of 12% in ductility and a drop of 50 MPa in UTS compared toTi0. After aging for 24 hours at 650C, the Ti2 system showed an increase in YS to 405 MPa, an increase to 590 MPa UTS, but a decrease in ductility to 22.9% from the previous 30.3%. On the other hand, the aged Al3 system showed an increase to 585 MPa at the yield point and a UTS of 882 MPa, while maintaining the ductility at 43.8%.

3.4. FRACTURE SURFACE ANALYSIS

Fracture analysis is shown in Figure 8. Figure 8 (a) and (b) show the Ti2 and Al3 samples aged for 24 hours at 650C, respectively. Figure 8 (a) shows a peak and valley with some pockmarks indicative of cup and cone failures though some porosity is interspersed. Some directional failure can also be determined by the failure lines originating from the bottom right failing towards to the highest peak in the center of the image. Figure 8 (b) shows a similar structure to Figure 8 (a) though with significantly higher concentration of cup and cone failure being visible in the bottom right. The same peaks and valleys are visible though a more constant slope of the fracture surface exists with fewer steps leading to a peak. The fractures are indicative of intergranular fracture rather than the typical intragranular fracture.

Fracture surface analysis is shown in Figure 8. A zoomed in version of each shows a closeup of the fracture to give a better idea of the fracture surface. Figure 8(a) shows the homogenized Ti0 system showing a ductile fracture surface. The fracture surface of the Ti0 shows a highly dimpled structure with few flat surfaces.

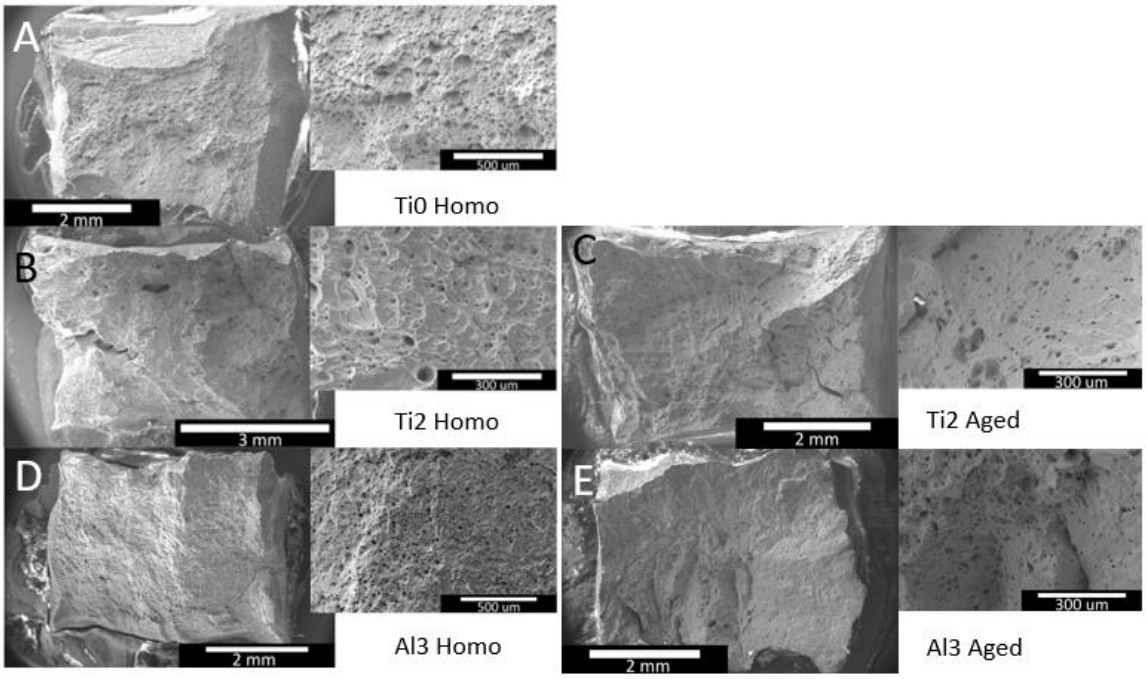

Figure 8. Shows the different fracture surfaces of the different alloys. A shows the fracture surface of the Ti0 system. B shows the fracture surface of the Ti2 system. C shows the aged fracture surface of the Ti2 system which can be seen is a lot smoother with few dimples. D and E show the Al3 system with Al3 homogenized showing a much more ductile matrix while E, the aged Al3 system shows a smoother surface with few dimples.

Figure 8 (b) and (c) show the homogenized and aged Ti2 systems. The Ti2 homo system shows similar behavior to the Ti0 fracture surface though large dimples are present with large precipitates being visible at the base of the dimples. Ti2 aged shows a large flat fracture surface with few dimples. Figure 8 (d) and (e) show the fracture surface of the Al3 system in both its homogenized and aged state respectively. The homogenized surface shows a large number of small dimples while the aged surface shows dimples but interspersed with large flat sections indicating a partially brittle partially ductile failure.

4. DISCUSSION

4.1. INITIAL MICROSTRUCTURE

Initial observations of the aged Ti2 and Al3 systems show that no microstructural changes in the Ti2 system after aging, while in Al3 subgrain formation is visible. Sub-grain formation in an unstrained matrix originates in defects induced due to precipitation or due to contracting during quenching.[29] The formation of hard precipitates exhibiting a hydrostatic strain on the ductile FCC matrix resulted in defect formation.[1] Due to the rapid temperature changes experienced during quenching, strain can be imparted in the matrix resulting in the formation of dislocations in both Ti2 and Al3 systems.[29] Due to the nature of the precipitates as an ordered FCC, it is expected that few geometrically necessary dislocations appear. Instead, it is probable that most dislocations appear due to quenching. Sub-grain formation after dislocation introduction is a function of defect diffusion resulting in the formation of defect clusters, lines, and eventually, low-angle grain boundaries which are pinned by precipitates as they migrate. [2,30]

4.2. TEM OF MICROSTRUCTURE

Both precipitate formation and the dislocation introduction discussed previously are also observable under STEM. The dislocations are only visible in the Ti2 system even after multiple zone axis were observed. It is theorized that the higher density of small precipitates in the Al3 system allows for the pinning of defects to form sub-grains as well as annihilation at boundaries.[23] As seen in Figure 1, sub grains form in the Al3 system. The sub-grain formation is also indicative of dislocation line formation and pinning. In

contrast, dislocation line buildup and entangling as seen in figure 4 shows that the Ti2 system does not exhibit as free dislocation movement, or the dislocations are not efficiently annihilating.

Dislocations motion allows many features to be explained. The high Mn in this alloy allows for a high stacking fault energy in this system. It is well known that high

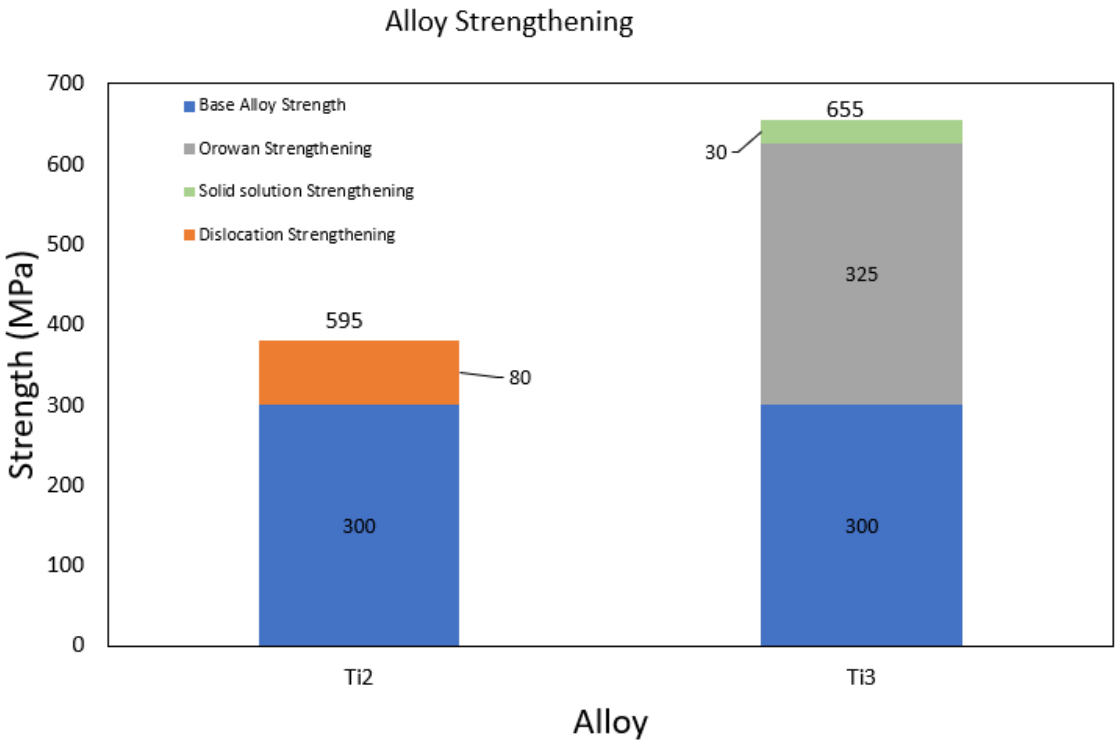

Figure 9. Strengthening analysis of both the Ti2 and the Al3 system. The Al3 system shows a significantly higher estimated strength, 3 times higher than that of the Ti2 system. Due to the size of the precipitates in the Ti2 system, their strengthening factor is negligible.

stacking fault energy austenitic alloys have rapid dislocation movement, and this is observable in this system. In Appendix 1 the dislocation motion is evident in the Ti2 system where the (111) slip planes are highlighted by strain due to the presence of

dislocations. While in the Al3 system these slip planes are also active, the high density of small precipitates inhibits this dislocation movement along the (111) plane forcing the dislocations to cross slip as they run into the precipitates. This impeding of dislocation movement eventually leads to buildup and subgrain formation. In the Ti2 system in contrast, due to the large precipitates, the dislocation motion is relatively uninhibited thus recrystallization occurs only at the grain boundaries. This dislocation buildup along the grain boundaries also causes grain boundary embrittlement leading to premature failure in samples.

4.3. MECHANICAL PROPERTIES

4.3.1. Strengthening Analysis. The strengthening analysis was done following the work of Luebbe et al. in. Using a volume fraction of 5.5% for the density of precipitates in the Al3 system as well as an average diameter of 10.7 nm for precipitates, it was determined that precipitation strengthening in the Al3 system was extremely high at 1350 MPa. This difference between the calculated strength and the actual strength will be discussed later. This can be seen in figure 9. In contrast, the Ti2 system experienced only very little strengthening which was attributed to the increased dislocation density. Dislocation densities can be seen in table 2.

Table 2 shows that during aging in the Al3 system, an overall reduction in dislocations was observed while in the Ti2 system, the dislocations increased slightly resulting in some dislocation strengthening. The slight increase in dislocations was linked to the formation of large precipitates requiring geometrically necessary dislocations to be formed.

Table 2. Dislocation density found in system and stage of processing with a reduction of dislocation density found in the Al3 system while a slight increase in the dislocation density is found in the Ti2 system due to the large precipitates exacting a hydrostatic pressure on the surrounding matrix.

	Dislocation Density (m^2)
FeNiMn20Cr20 Ti2Al1 Homo	4.04×10^{14}
FeNiMn20Cr20 Ti2Al1 Aged	7.72×10^{14}
FeNiMn20Cr20 Ti1Al3 Homo	5.20×10^{14}
FeNiMn20Cr20 Ti1Al3 Aged	1.05×10^{14}

4.3.2. Hardness. Figures 6 (a) and (b) reveal insights into the kinetics of precipitate formation are changed dramatically with a 100C increase in temperature. The 100C change makes the system viable, with the effect of 12+ hours of aging now achieved in a maximum of 1 hour improving its feasibility as a commercial product. More studies need to be performed before definitive answers on temperature stability can be given, but the observed lack of change in the hardness implies that high temperature strength is a possibility with further studies focusing on temperature stability of the precipitates as well as the matrix.

4.3.3. Tensile. The tensile data in Figure 6 shows Al3 exhibits high strength and high ductility. The negligible ductility change paired with a significant increase in hardness after aging in the Al3 system demonstrate the versatility of the current high entropy alloy supported by precipitation hardening. Results show that the addition of

Ti1Al3 is more beneficial than that of Ti2Al1 due to the change in precipitates. Both systems show the formation of L12 in XRD though the volume and distribution is vastly different, due to the large networked precipitates acting as both stress concentrations the Ti2 system experiences failure significantly before Al3 The Ti2 system experiences failure in both the homogenized state and the aged state due to the formation of larger precipitates in the aged state but also due to segregation of the L12 forming elements to grain boundaries as described by Liu et al.[25] Though segregation on a macro scale was not observed nor grain boundary preferential formation of L12 more work is required to confirm this theory.

Comparing the Ti2 system with the Ti0 and Al3 systems shows formation of precipitates during homogenization is not necessarily happening. Initial formation of precipitates does not occur with minimal differences being associated with solution strengthening. The reduction of strength is as previously attributed to grain boundary segregation of L12 forming elements. Pre- and post- aging in the Al3 system show evident differences in the UTS, YS, and ductility. The Al3 system shows a UTS increase from 540 MPa to 882 MPa with near no ductility loss. This change can be explained as a function of the initially millimeter-sized, effectively strain free, allowing a large buildup of dislocations before dislocation pinning and conglomeration occurs. The large difference between the calculated strength in the strengthening analysis vs the tensile data is due to the type of failure. A larger image of a separate fracture surface can be seen in Appendix 2 where the intergranular failure experienced by the sample is evident. The calculation of grain strengthening does not account for grain boundary strength thus overestimating the strength of the material. This problem may be mitigated in future work

by a reduction in the grain size through processing. While the dislocations introduced during homogenization form dislocations clusters and eventually sub-grain boundaries they do not, in the numbers introduced, change the ductility as even the sub-grains formed are still hundreds of microns in diameter. Further more, due to the relatively dislocation free matrix the already present dislocations have little effect on the ductility.[31,32]

4.4. FRACTURE SURFACES

While tensile testing shows the difference between the different alloys well, the fracture surfaces reveal another aspect of study highlighting the effect of the different aging conditions. Figure 7 (a) shows the Ti0 system fracture surface. This fracture surface has no major features besides the well dimpled fracture surface. It is important to note that similar features exist in both the homogenized Ti2 and Al3. The main difference being that the dimple size in the Ti2 system is on average larger as well as the flaws in the base of each dimple are angular and embedded rather than rounded which is seen in both the Ti0 and the Al3 system. These are also in line with the precipitates seen in the TEM images of the Ti2 system. The reduced strength can be lead back to two major points, the lack of precipitate strengthening, as well as the fracture of the large precipitates as observed by Wu. 2020 where the large y' precipitates acted as fracture initiation sites.[33]

While hard to observe, the fracture surfaces are not flat or even in a single plane. The Ti2 homogenized as well as both the aged samples broke at complex angles with cliffs and sharp facets rather than in a continuous plane. For instance, in the Ti2 homo,

the highest point of the fracture surface is approximately 3 inches higher than the lowest point.

These fractured surfaces tell an interesting story about the effect of the precipitates. The changes in precipitates cannot obviously be seen in the fracture surfaces, both the aged systems as well as the homogenized systems are comparable to each other and small differences like the size of the dimples in the Ti2 homogenized system are the only indication of differences between the systems. The aged systems also look similar with only the number of dimples being the defining feature differentiating the two. The slip plane activation that is visible in figure 4 as well as appendix 1 can also be seen in appendix 2 where the Ti2 system exhibits the slip planes on the dimple surface. The macroscopic as well as microscopic slip plane activation shows the dislocation movement planes.

5. CONCLUSIONS

The differences seen in the Ti2 and Al3 systems and how they oppose each other can all be unified when looking at the precipitates, their morphology, and their distribution. The Ti2 precipitates are significantly larger than those of the Al3 system. While the larger precipitates mildly contribute to the strength and hardness , they are also more likely to promote strain concentration which initiates the formation of cracks.

Conclusions

This study focused on the effect of ageing on the FeNiMn20Cr20 Ti_xAl_y alloy. Two ratios, Ti2Al1, and Ti1Al3 were compared in terms of mechanical properties and precipitates formation:

- Both the Ti2 and the Al3 system form L_{12} precipitates but the size, morphology, and distribution are vastly different.
- High strength (882 MPa) and high ductile (45.7%) was achieved in the Al3 subjected to ageing at 650C for 24 hours after ageing.
- The discovery of a strong and ductile alloy with potential as a relatively high temperature alloy based on precipitation temperatures is an exciting prospect. More studies can yield high temperature stability as well as the potential for this alloy to be produced by industrial processes in a scalable manner.

ACKNOWLEDGEMENTS

This research was supported by the U.S. Nuclear Regulatory Commission Faculty Development Program (award number NRC 31310018M0044) and by a research grant (award number 2207965) from U.S. National Science Foundation. Materials Research Center at Missouri University of Science and Technology is acknowledged for providing access to electron microscopy.

REFERENCES

1. Yeh JW, Chen SK, Lin SJ, et al. Nanostructured high-entropy alloys with multiple principal elements: Novel alloy design concepts and outcomes. Adv Eng Mater. 2004;6(5):299-303+274. https://doi.org/10.1002/adem.200300567

2. Tsai KY, Tsai MH, Yeh JW. Sluggish diffusion in Co-Cr-Fe-Mn-Ni high-entropy alloys. Acta Mater. 2013;61(13):4887–4897. https://doi.org/10.1016/j.actamat.2013.04.058

3. Miracle DB, Senkov ON. A critical review of high entropy alloys and related concepts. Acta Mater. 2017. https://doi.org/10.1016/j.actamat.2016.08.081

4. Tsai MH, Yeh JW. High-entropy alloys: A critical review. Mater Res Lett. 2014;2(3):107–123. https://doi.org/10.1080/21663831.2014.912690

5. Shi T, Lei PH, Yan X, et al. Current development of body-centered cubic high-entropy alloys for nuclear applications. Tungsten. 2021;3(2):197–217. https://doi.org/10.1007/s42864-021-00086-6

6. Wang X, Guo W, Fu Y. High-entropy alloys: Emerging materials for advanced functional applications. J Mater Chem A. 2021;9(2):663–701. https://doi.org/10.1039/d0ta09601f

7. Miracle DB, Miller JD, Senkov ON, Woodward C, Uchic MD, Tiley J. Exploration and development of high entropy alloys for structural applications. Entropy. 2014;16(1):494–525. https://doi.org/10.3390/e16010494

8. Senkov ON, Senkova S V., Woodward C. Effect of aluminum on the microstructure and properties of two refractory high-entropy alloys. Acta Mater. 2014;68:214–228. https://doi.org/10.1016/j.actamat.2014.01.029

9. He F, Chen D, Han B, et al. Design of D0 22 superlattice with superior strengthening effect in high entropy alloys. Acta Mater. 2019;167:275–286. https://doi.org/10.1016/j.actamat.2019.01.048

10. Ma E, Wu X. Tailoring heterogeneities in high-entropy alloys to promote strength–ductility synergy. Nat Commun. 2019;10(1):1–10. https://doi.org/10.1038/s41467-019-13311-1

11. Zheng F, Zhang G, Chen X, et al. A new strategy of tailoring strength and ductility of CoCrFeNi based high-entropy alloy. Mater Sci Eng A. 2020;774(January):138940. https://doi.org/10.1016/j.msea.2020.138940642513zy3

12. Xia S qin, Wang Z, Yang T fei, Zhang Y. Irradiation Behavior in High Entropy Alloys. J Iron Steel Res Int. 2015;22(10):879–884. https://doi.org/10.1016/S1006-706X(15)30084-4

13. Ravi Kumar B. Influence of crystallographic textures on tensile properties of 316L austenitic stainless steel. J Mater Sci. 2010;45(10):2598–2605. https://doi.org/10.1007/s10853-010-4233-x

14. Hadraba H, Chlup Z, Dlouhy A, et al. Oxide dispersion strengthened CoCrFeNiMn high-entropy alloy. Mater Sci Eng A. 2017;689(December 2016):252–256. https://doi.org/10.1016/j.msea.2017.02.068

15. Ming K, Bi X, Wang J. Realizing strength-ductility combination of coarse-grained Al0.2Co1.5CrFeNi1.5Ti0.3 alloy via nano-sized, coherent precipitates. Int J Plast. 2018;100(October 2017):177–191. https://doi.org/10.1016/j.ijplas.2017.10.005

16. Chen D, He F, Han B, et al. Synergistic effect of Ti and Al on L12-phase design in CoCrFeNi-based high entropy alloys. Intermetallics. 2019;110(May):106476. https://doi.org/10.1016/j.intermet.2019.106476

17. Cantor B, Chang ITH, Knight P, Vincent AJB. Microstructural development in equiatomic multicomponent alloys. Mater Sci Eng A. 2004;375–377(1-2 SPEC. ISS.):213–218. https://doi.org/10.1016/j.msea.2003.10.257

18. Wu P, Gan K, Yan D, Fu Z, Li Z. A non-equiatomic FeNiCoCr high-entropy alloy with excellent anti-corrosion performance and strength-ductility synergy. Corros Sci. 2021;183(February):109341. https://doi.org/10.1016/j.corsci.2021.109341

19. Hou X, Zhang X, Liu C, et al. Effects of Annealing Temperatures on Mechanical Behavior and Penetration Characteristics of FeNiCoCr High-Entropy Alloys. Metals (Basel). 2022;12(11). https://doi.org/10.3390/met12111885

20. Yang T, Zhao Y, Liu W, Kai J, Liu C. L12-strengthened high-entropy alloys for advanced structural applications. J Mater Res. 2018;33(19):2983–2997. https://doi.org/10.1557/jmr.2018.186

21. Gwalani B, Soni V, Choudhuri D, et al. Stability of ordered L12 and B2 precipitates in face centered cubic based high entropy alloys - Al0.3CoFeCrNi and Al0.3CuFeCrNi2. Scr Mater. 2016;123:130–134. https://doi.org/10.1016/j.scriptamat.2016.06.019

22. Huang S, Ghosh G, Li X, Ilavsky J, Teng Z, Liaw PK. Effect of Al on the NiAl-type B2 precipitates in ferritic superalloys. Metall Mater Trans A Phys Metall Mater Sci. 2012;43(10):3423–3427. https://doi.org/10.1007/s11661-012-1318-y

23. Velikodnyi AN, Voyevodin VN, Kalchenko AS, et al. Impact of nano-oxides and injected gas on swelling and hardening of 18Cr10NiTi stainless steel during ion irradiation. J Nucl Mater. 2022;565:153666. https://doi.org/10.1016/j.jnucmat.2022.153666

24. Klueh RL, Shingledecker JP, Swindeman RW, Hoelzer DT. Oxide dispersion-strengthened steels: A comparison of some commercial and experimental alloys. J Nucl Mater. 2005;341(2–3):103–114. https://doi.org/10.1016/j.jnucmat.2005.01.017

25. Liu L, Zhang Y, Wu G, et al. The effect of Al/Ti ratio on the evolution of precipitates and their effects on mechanical properties for Ni35(CoCrFe)55AlxTi10−x high entropy alloys. J Alloys Compd. 2022;906:164291. https://doi.org/10.1016/j.jallcom.2022.164291

26. Wu J, Liu X, Zhu H. Achieving strength-ductility balance in a casting non-equiatomic FeCoNi based medium-entropy alloy via Al and Ti combination addition. J Mater Res Technol. 2023;23:627–636. https://doi.org/10.1016/j.jmrt.2023.01.035

27. Luebbe M, Duan J, Zhang F, et al. Materials Science & Engineering A A high-strength precipitation hardened cobalt-free high-entropy alloy. Mater Sci Eng A. 2023;870(February):144848. https://doi.org/10.1016/j.msea.2023.144848

28. Hoffman A, He L, Luebbe M, et al. Effects of Al and Ti Additions on Irradiation Behavior of FeMnNiCr Multi-Principal-Element Alloy. Jom. 2020;72(1):150–159. https://doi.org/10.1007/s11837-019-03871-4

29. You A, Be M, In I. Quench - Induced Defect Structure in Al - 6.5 - at.% Zn. 2003;2611(July 1992):2603–2611.

30. Sedlák R, Blum W, Kratochvi J, Sedla R. Subgrain Formation during Deformation: Physical Origin and Consequences. 2002;33(February):319–327.

31. Blum W. Role of Dislocation Annihilation during Steady-State Deformation. Phys Status Solidi. 1971;45(2):561–571. https://doi.org/10.1002/pssb.2220450219

32. Wang L, Zhang Z, Ma E, Han XD. Transmission electron microscopy observations of dislocation annihilation and storage in nanograins. Appl Phys Lett. 2011;98(5). https://doi.org/10.1063/1.3549866

33. Dauskardt RH, Haubensak F, Ritchie RO. On the interpretation of the fractal character of fracture surfaces. *Acta Metall Mater*. 1990;38(2):143–159. https://doi.org/10.1016/0956-7151(90)90043-G

III. SCALE CASTING OF MULTI-PRINCIPAL ELEMENT ALLOY

Hans Pommerenke, Rogerio Cardoso, Matthew Luebbe, Viraj Ashok, Visharad Jalan, Michael Piston, Katelyn Kiser, Kyle Burke, Ronald O'Malley, Haiming Wen*,

Department of Materials Science and Engineering, Missouri University of Science and Technology, Rolla, MO 65401, USA

ABSTRACT

Due to the relatively new nature of most work on multi-principal element alloys (MPEAs) most work has focused on the laboratory scale work rather than larger castings. For research purposes this is great as almost all literature focuses on smaller batch sizes with high control over atmosphere, raw materials, and casting quality. The next step though, transforming a material with good properties in the laboratory to a product capable of being used has been all but ignored. In this work, 80 lbs of an FCC precipitation strengthened alloy Fe30Ni30Mn20Cr20 Ti3Al1 was cast using standard steel casting techniques. This alloy was investigated for its properties as well as for inclusion formation during casting. The alloy cast resulted in properties lower in both ductility and strength than its vacuum induction cast counterpart, but strong indications were found suggesting modern steel techniques can cast MPEAs with few changes taking the first step in scale casting of MPEAs.

1. INTRODUCTION

The field of a multi-principal element alloys(MPEAs) (often called High Entropy Alloys (HEAs)) is a quickly growing field. First proposed in 1996[1] and really picking up steam in 2004[2], the characteristics of MPEAs lend themselves to the growing market for specialty alloys.[3, 4] Due to their nature of taking advantage of the properties of multiple elements, MPEAs have found use in many different applications.[5, 6] From structural materials to wear and corrosion resistant coatings, to specialty industries such as the nuclear industry MPEAs offer the ability to be tailored to each purpose, outperforming the steels and super alloys currently used.[7–9]

MPEAs or HEAs are often defined by a short list critical characteristics.[10, 11]

1. The use of 5 or more principal alloys in the range of 5-35 at% with alloying elements under 5%.
2. The high entropy effect, which suggests that due to the high mixing entropy of these alloys, lower energy phases are more likely to form resulting in simple, single-phase structures such as FCC, BCC, or HCP.[12–14] While not the only phases forming, MPEAs with these simple single phases have shown promising results and often are found to be enhanced with precipitation strengthening. [15–17]
3. Lattice-Distortion effect which focuses on the random position of atoms throughout a structure. This results in a distorted lattice which effects the properties from changing entropy to increased hardness and other properties changing though alloy to alloy these changes.

4. “Cocktail effect” which focuses on the synergistic effects of different elements in a mixture having a positive effect on the overall properties of an alloy. Small effects such as the addition of chrome to an iron alloy increasing the corrosion resistance are well known but the complex nature of MPEAs allows surprising and new effects to be expected and other factors such as microstructure and secondary phases also play a large roll.[18]

While the field of MPEAs has grown rapidly in the recent past, the focus has been on small amounts of material and controlling every aspect from pure starting material[19–21] to perfect atmosphere control through the use of vacuum induction casting or arc melting [19–21], and finally to using muffle furnaces for all heat treatments. While for the scientific world this is great and many good advancements have been shown, especially in the world of structural materials or specialty alloys while small scale results are promising being able to produce the material is absolutely necessary. Little to no work has been performed on scale castings of MPEAs. From inclusion analysis to testing the possibilities of using modern steel casting techniques to cast MPEAs the lack of knowledge holds back a lot of research from leaving the lab and becoming a product reality. [10, 11]

In this work, the scalability of MPEAs in a modern production environment was investigated. Using a modern 100lb steel making induction furnace 80lbs of an (FeNiMn20Cr20)96 Ti1Al3 alloy were cast. Detailed notes were taken during the casting to show that modern steel casting techniques are up to the task of casting MPEAs without the creation of specialty equipment nor time intensive preparations. A detailed inclusion

analysis was performed and properties compared to the same alloy cast in a vacuum induction furnace.

2. EXPERIMENTAL PROCEDURE

2.1. GOAL COMPOSITION

The goal composition if FeNiMn20Cr20 Ti1Al3 can be seen in Table I. Initial materials added to the crucibles of each furnace can also be seen in Table I. All raw materials were of high purity with Induction iron being used as an Iron source and Nickel shot being used as the nickel source. All other raw materials were 99.5% pure though no nitrogen, sulfur, or oxygen content were noted of the raw material.

Table 1. The at% and wt% of the alloy that was cast as well as the amount of raw materials that were added to each furnace.

	Fe	Ni	Mn	Cr	Ti	Al
At. %	29	29	19	19	3	1
Wt. %	29.4	29.8	18.9	18.8	2.6	0.5
Vacuum Induction Furnace (g)	1030	1090	660	630	91	17
Foundry Induction Furnace (g)	10660	10820	6880	6870	950	180

2.2. VACUUM INDUCTION MELTING

Vacuum induction melting (VIM) was performed in a customized vacuum induction furnace using an Induction technology corporation induction furnace Model: ITC-20-96-N. A large roughing vacuum pump with a 3 hp motor is connected to the

vacuum induction furnace. Oxygen content was measured using a custom system with sensors capable of detecting oxygen content under 8 torr total pressure. Oxygen pressure was measured using 2 different sensors. One in the main chamber and one near the pump. This system can be seen in figure 1. The induction coil pack in the vacuum induction furnace had a 10 lb alumina crucible installed with a layer of refractory concrete to act as a spout as well as to protect the coil pack from molten metal during pouring. The mold for this casting was made of no-bake epoxy-sand mold with a steel quench block at the bottom to promote directional solidification and did not have a filter agianst impurities.

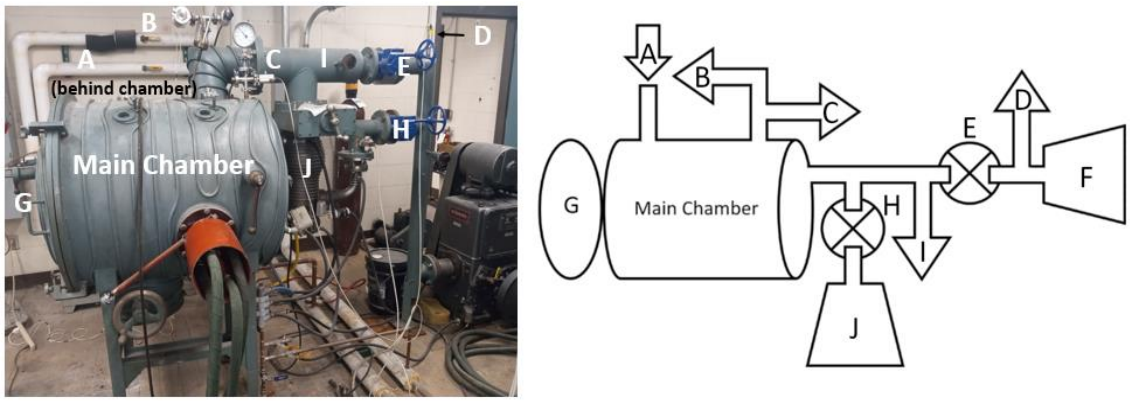

Figure 1. A diagram of the vacuum induction furnace. The main chamber has 2 inputs plus the main door and two small windows and a passthrough for electrical lines. A: argon input line, B: one directional bleed valve, C: Oxygen sensor 2, D: Oxygen sensor 1, E: Roughing pump valve, F: Roughing Pump, G: Main chamber door, H: Diffusion pump valve, I: Main vent, J: Diffusion pump.

In this study, VMI was performed by adding all the charge at the same time into the crucible. As the top of the charge is outside of the induction coils, magnetic materials were mixed throughout the system to minimize the risk of bridging.The rouging pump was then turned on to pump down the furnace. Once the pressure had reached a steady

state (1.14 torr) as indicated by oxygen sensor C valve E was closed while valve A was opened to allow argon to backfill the main chamber. The argon used was industrial grade argon. This process was performed 3 times in total with a lower oxygen content (as measured by oxygen sensor C). Each itterative step resulting in a lower minimum oxygen content with the lowest measured being at 1.03 torr. Once the minimum oxygen content was reached the system was backfilled with argon and the roughing pump was turned off. Valved E was also closed. Due to leaks in the chamber the diffusion pump was not turned on as the maximum allowable pressure for the diffusion pump was not reached.

Initial heating began once the system was over-pressurized and a steady over-pressure was established. Heating was performed in 3 kW increments starting at 3 kW and increasing by 3kW every 10 minutes to avoid any thermal cracking in the crucible as well as thoroughly give the raw material time to fully reach temperature. Melting of the magnetic material began approximately at 12 kW after about 2 minutes at temperature. After melting began the system was raised to 14 kW to ensure a proper super heat. No temperature measurments were possible as the system does not allow for a thermocouple to be used more than once and a laser pirometer was not installed at the time. Due to some bridging events occuring, the curcible was tilted so the liquid touched the bridging material melting the material. This melting process was took approxiametly 15 minutes once the final temperature was reached. Some vapors were also released during this time in the form of a grey-green gas which increased the overall pressure as well as obscured vision through vision windows in the main chamber. Once all material was fully melted preperation for pouring was performed. The pouring process involved turning off the induction coils and tipping the internal induction coil pack using a handle on the outside

of the main chamber. The liquid was then poured into the mold which had been pre-placed in the chamber prior to sealing. After pouring valve A and B were closed. The main chamber door was then opened and the main chamber allowed to vent. This included vapor released during melting as well as excess argon. After allowing the system to cool off the mold was removed and broken open resulting in a as-cast high entropy alloy rectangle.

2.3. FOUNDRY INDUCTION MELTING

The goal was to cast approxiametly 80 lbs to cover a solidification spiral, a wheel center, 6 ‘y’-block molds, and pig molds to pour the extra molten charge. The wheel center was used to determine the feasability of casting complex parts with a high entropy alloy. The 6 ‘y’-blocks were cast to create tensile and charpie samples and to observe the microstructure of the as-cast microstructure. The solidification spiral as well as the ‘y’-blocks all had a ceramic filter to filter out inclusions from casting.

‘Y’-blocks for this casting had a rectangular section of 25mm x 60mm x 127mm with a large rectangular riser of 40mm x 29mm x 130 mm to minimize porosity. These blocks were bottom filled from a central pouring spout with 10mm x 10mm channels. The different molds were lined up in fill order: solidification spiral, wheel, set of 4 y-blocks, set of 2 y-blocks, pig molds.

Melting procedure was documented; multiple samples taken at different times to trace additions and processing. The spout and protective layer on the induction coils was the same as that used in the vacuum induction system. Molds were produced using the same resin-sand system as in the vacuum induction melting. To begin the melting process, nickel, iron, and chrome were heated together to mitigate the loss of these

elements due to their melting point. Once the system was fully liquid Mn, additions were added. The first Mn additions were added at a temperature of 1527 °C when ¼ of the Mn was added. The Mn was stirred into the molten metal with a low carbon steel stirring rod. . The temperature was found to be 1625 °C at the time of the vacuum and OES samples. Upon the Ti additon, a sample was taken 3 minutes after the last temperature measurment by hand ladle for a solidification cup in addition to an additional temperature measurment which showed the furnace had cooled during the time to 1531 C. The furnace was then tapped into the ladle with the aluminum being added when the ladle was 1/3 full of molten steel. A second solidification cup was taken at this point as well as a temperature measurement showing the temperature was 1529 °C. Pouring then commenced in the mold order until every mold was no longer filling. Microstructure and solidification cup data can be seen in figure 2. Table 2 contains the elemental data for the two OES samples.

Samples were placed into a furnace at 1200C for 5 hours for homogenization. Homogenization was performed using both a steel bag to protect the sample from oxidizing as well as a flowing argon blanket during the homogenization process. After homogenization samples were subequently quenched in mildly agitated water.

Aging for all samples was performed in a tube furnace with flowing argon atmosphere for 24 hours at 750 °C as shown in previous work to be the most effective . The 24 hours was used to ensure results are comparable, in terms of processing, with previous and future work. Be that as it may, previous work has shown peak strength can be reached after only 1 hour of homogenization at 750 °C . After homogenization samples were air cooled.

2.4. MICROSTRUCTURAL CHARACTERIZATION AND MECHANICAL TESTING

Characterization of all samples was performed using an Fisher Scientific Axia ChemiSEM scanning electron microscope (SEM) under 30 kV with 1.5 nA current while all automated feature analysis (AFA) was performed on an Aspex 1020. Samples for SEM were polished using SiC paper using grits: 320, 600, 800, and 1200. Following SiC paper, samples were polished using diamond paste using 9 um, 3 um, 1 um, 0.1 um, and finally 0.02 colloidal silica. To avoid Si contamination during AFA samples were not polished past 0.1 um diamond paste to ensure no contamination by the Si.

Uniaxial tensile tests were performed on a LandMark MTS load frame with a 250 kN load frame; Samples were cut using water jet from machined 'Y' block samples. In conformity with the ASTM E8 standard, sub-size tensile specimens were used. The tests were carried out at the rate of 0.05 mm/sec until failure. Elongation of the samples was measured using a laser extensometer. For each condition, namely homogenized and aged, of both types of casting, 3 samples were tested to ensure representative data. In the case of non-vacuum melting, samples were taken from different 'Y'-blocks to ensure standardization across different castings from the same heat.

Hardness testing was performed on the fracture toughness samples using a Wilson hardness tester Rockwell 574. 10 impact points were taken per sample. Charpy V-notch (CVN), following ASTM E23, impact toughness was investigated using Tinius Olsen Model 892 Charpy impact tester in multiple states: as- homogenized at room temperature, as-homogenized at -40C, aged at room temperature, and aged at -40 °C. Each fracture test was performed 3 times.

For oxygen and nitrogen testing, samples weighing between 0.5 – 1 g were cut from the samples taken during alloying element addition as well as from the final casting. 3-5 samples were taken from each stage. The testing was performed on a N/O LECO TC500.

3. RESULTS

Table 2 shows the results of optical emissions spectroscopy (OES) analysis One can note a change in casting composition throughout the addition of alloying elements, mainly, the presence of both Al and Si initially though in small amounts. Only in the final casting are any variances seen from the desired amount to the actual amount in the casting. Ti is seen to lose approximately 0.6 wt% between its addition to the final casting. All other elements are within margin of error with the exception of Nickel which over the casting loses 1.2 wt% as well as an initially low starting wt% of 29.2 rather than the expected 29.8 wt%.

Table 3 shows the comparison between the two different melting. Due to the nature of the vacuum induction casting, sampling upon alloy additions was not possible. While the same weight percentage of starting material was added to both castings, significantly different final compositions can be seen.

Table 2. Shows the elemental analysis throughout the alloying addition processes.

	Foundry Induction Cast (wt%)		
Element	FeNiMn20Cr20 As Cast	FeNiMn20Cr20 Ti3 As Cast	FeNiMn20Cr20 Ti3Al1 As Cast
Al	0.1 ± 0.1	0.1 ± 0.1	0.7 ± 0.2
Si	0.4 ± 0.1	0.4 ± 0.1	0.3 ± 0.1
S	0.0 ± 0.0	0.1 ± 0.0	0.0 ± 0.0
Ti	0.0 ± 0.0	2.7 ± 0.2	1.9 ± 0.2
Cr	19.9 ± 0.6	19.2 ± 0.4	19.6 ± 0.4
Mn	19.9 ± 0.5	19.6 ± 0.3	19.3 ± 0.3
Fe	30.5 ± 0.7	29.8 ± 0.3	30.4 ± 0.4
Ni	29.2 ± 0.3	28.3 ± 0.4	27.8 ± 0.4

Table 3. Shows the composition of the homogenized and aged systems for both the foundry induction cast and vacuum induction cast systems.

Element	Foundry Induction Cast		Vacuum Induction Cast	
	FeNiMn20Cr20 Ti3Al1 Homo	FeNiMn20Cr20 Ti3Al1 Aged	FeNiMn20Cr20 Ti3Al1 Homo	FeNiMn20Cr20 Ti3Al1 Aged
Al	0.6 ± 0.2	0.6 ± 0.2	1.4 ± 0.1	1.4 ± 0.1
Si	0.4 ± 0.1	0.3 ± 0.1	0.3 ± 0.1	0.4 ± 0.1
S	0.0 ± 0.0	0.0 ± 0.1	0.0 ± 0.0	0.0 ± 0.0
Ti	2.1 ± 0.2	2.1 ± 0.2	0.9 ± 0.1	1.0 ± 0.1
Cr	19.2 ± 0.3	19.2 ± 0.3	19.8 ± 0.2	19.7 ± 0.2
Mn	19.4 ± 0.2	19.2 ± 0.3	16.4 ± 0.2	16.5 ± 0.2
Fe	30.0 ± 0.1	30.2 ± 0.3	30.2 ± 0.2	30.3 ± 0.3
Ni	28.3 ± 0.2	28.2 ± 0.3	30.5 ± 0.3	30.7 ± 0.4

The vacuum induction system held significantly larger amounts of Al as well as larger than the initially added Al amount, which will be discussed in later sections. . Mn

content in the vacuum induction cast system is also reduced from the desired amount. This difference is also discussed further in this work.

Table 4 shows the content of N and O of both castings. For the foundry cast system, since the samples were taken at various stages, there are O and N readings for the base alloy as well as both the alloying agents. For the vacuum induction cast system, the only readings are from the final casting. One can note the stark difference between the two types, with the vacuum induction casting having a factor of hundreds difference in the oxygen content while a factor of ten higher N content in the foundry cast system vs the vacuum induction system. The samples taken at various stages in the foundry casting shows the addition of Ti raised the oxygen content by 0.6 wt%. N on the other had was shown to be steady throughout the entire casting process.

Table 4. Shows the Nitrogen and Oxygen content throughout the alloying additions. In addition, the homogenized vacuum cast sample is shown as a comparison. No intermediate steps were included due to the nature of the vacuum induction furnace.

	Foundry Cast		Vacuum Induction Cast	
Alloy	**O% (wt%)**	**N% (wt%)**	**O% (wt%)**	**N% (wt%)**
FeNiMn20Cr20	0.092 ± 0.015	0.012 ± 0.000	--	--
FeNiMn20Cr20 Ti3	0.712 ± 0.102	0.013 ± 0.008	--	--
FeNiMn20Cr20 Ti3 Al1	0.703 ± 0.120	0.012 ± 0.001	0.003 ± 0.0001	0.0038 ± 0.0005

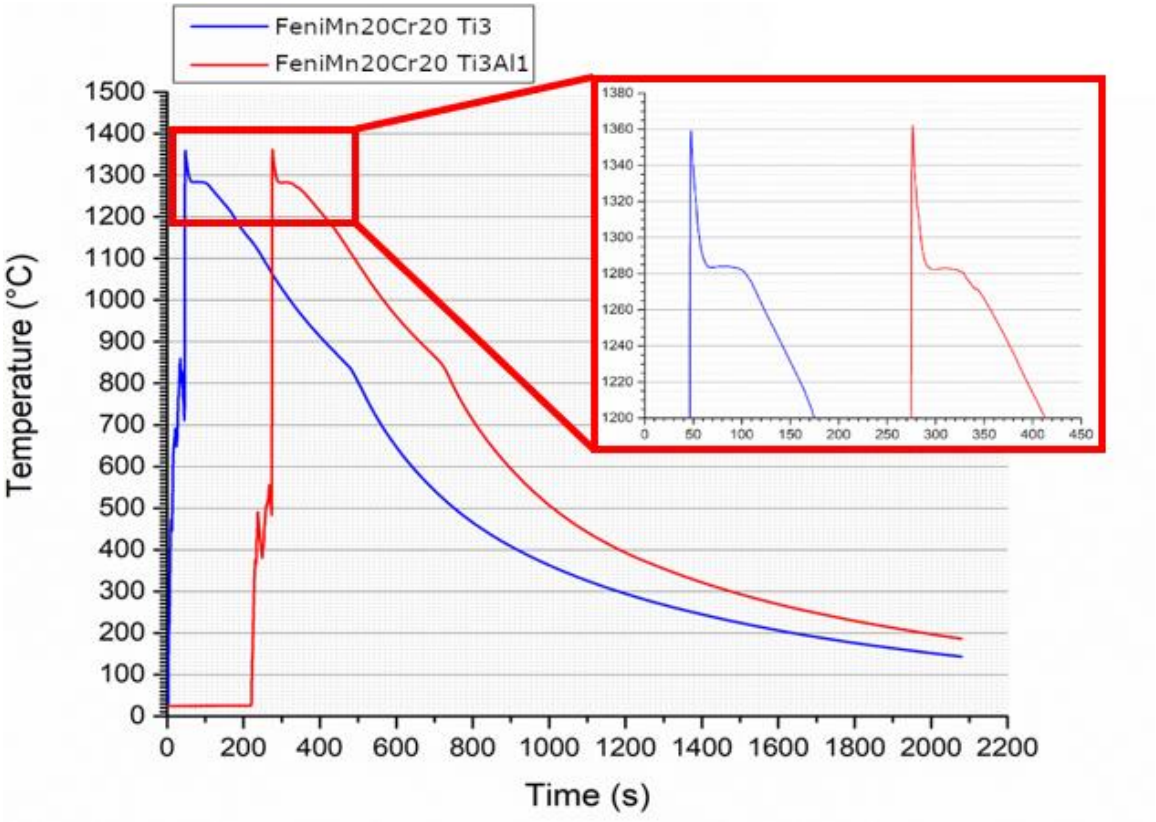

Figure 2. Shows the solidification data for both the Al3 and the Ti1Al3 systems. The Al addition is seen to be negligible here. The small slope change in the Ti1Al3 graph at 1250C is due to a vibration on the foundry floor while the large slope change at 850C is due to the solidification cups breaking.

Figure 2 shows the data from solidification cups taken after the addition of both Ti and Al. The solidification temperature of both systems is around 1283 °C with only a small reduction in solidification temperature due to the Al addition. A small hitch can be observed in the Ti1Al3 casting due to a vibration of the solidification cup while going through the casting procedures. A small change in the gradual slope of the systems at

around 840-850C stems from the breaking of the ceramics making up the solidification cups and is a known feature of the cups used.

3.1. INCLUSIONS

3.1.1. Inclusion Characterization. Initial characterization of inclusions was performed by hand with rough numbers developed to determine general rules of characterization for use in the automated feature analysis system. The automated precipitate analysis rules used for the precipitate analysis can be seen in Table 5. For elements that are intentionally added, a 3-5 wt% range is given to allow for variations in the dendritic structure formed in the as-cast system as well as enrichments found throughout the systems. Oxides were found to be very rich in oxygen, resulting in the larger than 5% oxygen classification. It's stipulated. However, that N and S were low on account of the complex nature of many inclusions, which is discussed in later sections. MnS and TiS were also found in large quantities; given their similar nature, Ti content was used as determining factor to ascertain the difference between each inclusion as both

Table 5. Shows the rules used to define inclusions during the automated analysis. The rules were generated by analysis done by EDS and looking at the type of inclusions formed by hand.

Inclusion Categorization Rules				
Oxide	O > 5%	N < 5%	S < 2%	
MnS	Mn > 25%	N < 5%	S > 2%	Ti ≤ 5%
MnS + TiS	Mn > 25%	N < 5%	S > 2 %	Ti > 5%
TiN	Ti > 5%	N > 5%	S < 2 %	

contained large amounts of sulfur and Mn is present throughout the matrix as well as most inclusions. TiN was often pure Ti and N, rendering them relatively easy to determine with minor amounts of S present in some inclusions.

3.1.2. Complex Inclusions. Due to the complex nature of many inclusions, they could not be included in the following ternaries. These complex inclusions were included in table 6 as this data is supplemented with data as determined by hand in conjunction

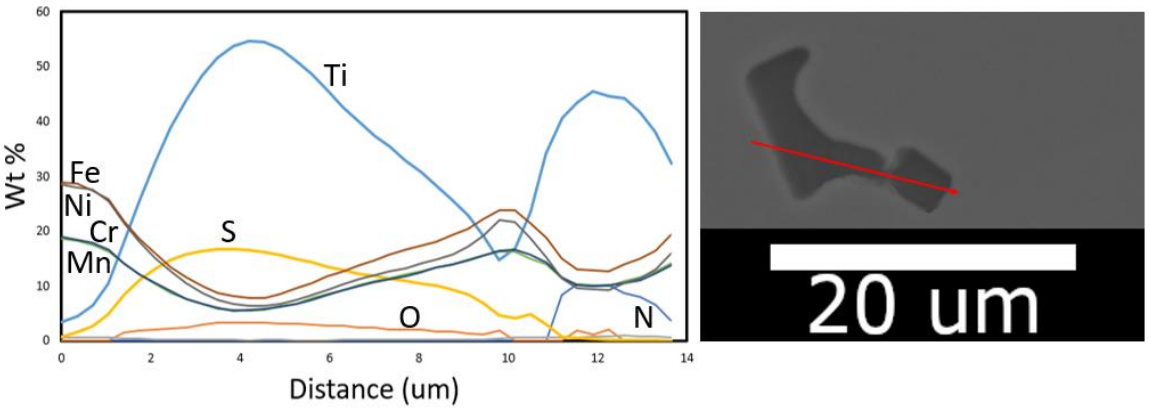

Figure 3. Shows the complex inclusions which can be found in the microstructure. These complex inclusions make automated feature analysis complicated as the automated system using contrast suggests these two inclusions are a single inclusion and rates it as a TiS inclusion rather than a TiS with a TiN inclusion.

with EDS. The complex inclusions, as can be seen in figure 3, often are multiple inclusions which have clustered together. Since AFA employs brightness/contrast thresholding to determine the area to be scanned, it can be complicated to distinguish inclusions automatically. Due to these complex inclusions, such as the inclusion shown in figure 3, which is a TiS particle with a small oxygen content conjoined with a TiN

particle, it's difficult to classify with the simple rules shown in table 5. For this reason, the addition of inclusions determined by hand is necessary in table 6-8.

Table 6. Shows inclusions by volume fraction throughout different alloying additions as well as processing conditions. The homogenization stage can be identified as a large contributor to the formation of inclusions.

FeNiMn20Cr20 Ti3Al1	Inclusion Type (volume fraction)				
	Porosity	Oxides	TiN	TiS	MnS
Filter	0.049	0.0028	0.0028	0.003	0.0049
No Filter	0.058	0.0262	0.219	0.0284	0.0283

3.1.3. Automated Inclusion Analysis. Table 6-8 shows the inclusions as well as porosity as determined by AFA. The data has been split into Tables 6-8 for ease of

Table 7. Shows the effect of the usage of a filter vs the usage of no filter in castings. The filters are shown to be effective at stopping inclusions from entering the casting.

Casting	Processing Condition	Inclusion Type (volume fraction)				
		Porosity	Oxides	TiN	TiS	MnS
FeNiMn20Cr20	As Cast	0.196	0.11	--	--	0.0004
FeNiMn20Cr20 Ti3	As Cast	0.056	0.0085	0.100	0.0072	0.0006
FeNiMn20Cr20 Ti3Al1	As Cast	0.049	0.0028	0.0028	0.003	0.0049
FeNiMn20Cr20 Ti3Al1	Homogenized	0.185	0.0194	0.2366	0.0039	0.0147
FeNiMn20Cr20 Ti3Al1	Homogenized and Aged	0.154				

readability. While it is hard to compare the samples taken during casting with the final product, it can be helpful to see the reduction of oxides with the addition of Ti and later Al. In addition, MnS only form a in large amounts during the casting and subsequent stages of processing. A comprehensive breakdown of different factors can be observed in tables 7 and 8. Table 7 shows the difference between the use of a filter during casting with a much higher volume fraction of TiN without a filter rather than with. All other inclusions also show a large reduction due to the filter. Table 8 compares the vacuum cast vs the foundry cast final products, showing that, during aging, the inclusion volume fraction lowers by 0.55 as well as across the board by all inclusions. TiS are only present in small quantities in the vacuum cast system.

Figures 3 and 4 show the ternaries for the inclusion analysis shown in Tabled 6-8. Oxide formation is favored in the FeNiMn20Cr20 base alloy though with the addition of Ti, TiN becomes the dominant inclusion in terms of volume fraction. Initial oxide formation favors a Mn oxide though matrix elements are all present in most inclusions. The Ti-N-Mn ternary shows that most TiN focuses on the 1:1 ratio with small deviations away from this ratio. After homogenization the TiN inclusion composition slowly shifts towards the Ti rich composition but after aging this change is reversed again to move towards the 1:1 ratio though with a larger amount of Mn present in the inclusions.

Figures 3 also shows an interesting trend with oxides after the initial reduction of oxide formation due to the addition of alloying elements. After the initial reduction in oxides, the oxides experience compositional clustering, narrowing down the type of oxides forming, which also shows a reduction in oxygen heavy oxides. In figure 4, which

focuses on the vacuum cast alloys, the same trends can be observed though the number of inclusions is vastly reduced.

Table 8. Shows the volume fraction of inclusions comparing the vacuum cast homogenized and aged to that of the foundry cast homogenized and aged.

FeNiMn20Cr20 Ti3Al1	Inclusion Type (volume fraction)				
	Porosity	Oxides	TiN	TiS	MnS
Vacuum Cast Homo	0.172	0.006	0.0943	0.000	0.002
Vacuum Cast Aged	0.166	0.001	0.0390	0.000	0.001
Foundry Cast Homo	0.185	0.0194	0.2366	0.0039	0.0147
Foundry Cast Aged	0.154				

The same compositional trends can also be observed with in the Mn-Cr-O ternary though in the N-Ti-Mn ternary the compositional change after aging, increased Mn content in the TiN, is not observable. Throughout all castings, the sulfide inclusions remain relatively stable, with a compositional clustering around the 2:1 ratio of M:S in both the Mn-S-O ternary as well as the Mn-S-Ti ternary. From this ratio, the inclusion composition moves towards the O or Ti rich compositional position.

3.2. MECHANICAL TESTING

3.2.1. Fracture Toughness. Table 9 shows the results of the CVN tests. The vacuum cast system exhibits twice the fracture toughness 215J vs 118 J in the foundry

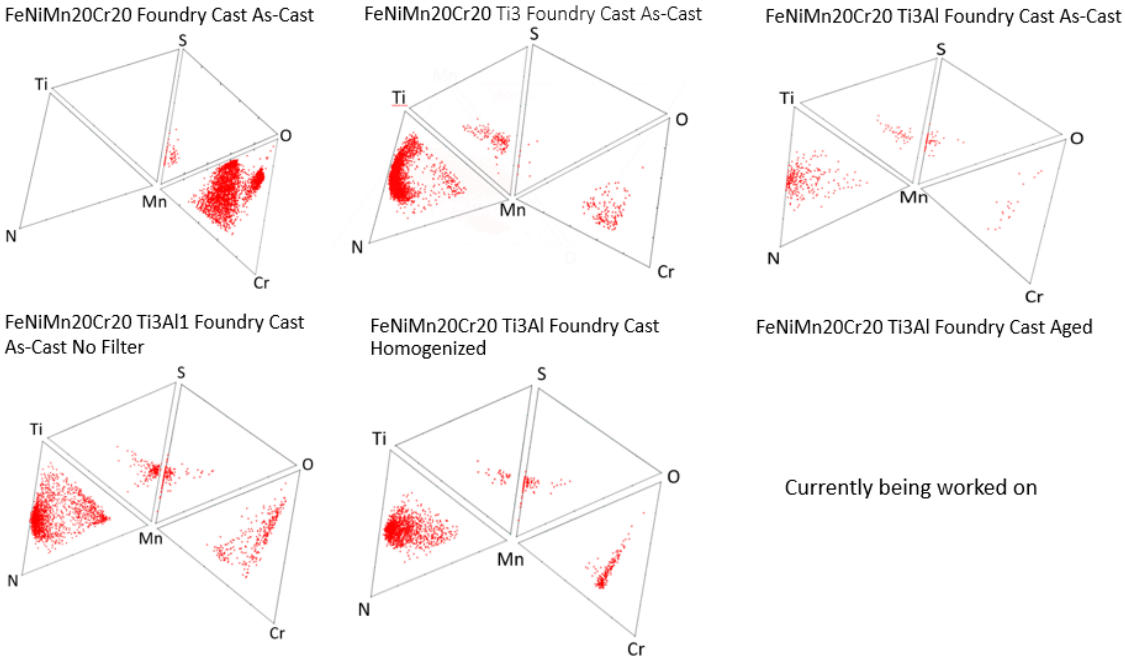

Figure 4. Shows the inclusion composition throughout processing states. The initial high oxide content is replaced by TiN after the addition of Ti to the melt. The effect of the filter vs no filter is also visible. The TiN and Mn-Cr-O ternaries show a change in composition of the inclusions which precipitated in homogenization rather than during the casting and cooling process.

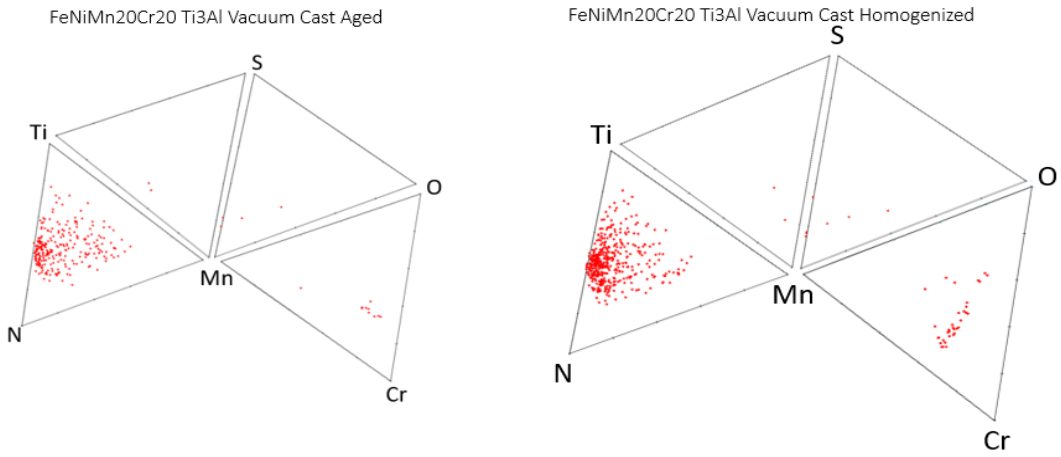

Figure 5. Shows the inclusion composition in the vacuum induction cast samples. The TiN composition after aging reflects the same shift that the TiN composition showed in the foundry cast system though it includes less Mn.

cast system. In the homogenized state, the vacuum cast exhibits a reduced hardness of 12 HV when compared to the homogenized foundry sample. CVN tests at -40C produce no major changes in either sample.

In the aged states, the foundry cast exhibits a brittle failure with only 11 J of breaking energy while the vacuum cast system exhibits a significantly higher breaking energy at 83J. The corresponding hardness change is also evident, with the foundry cast system showing a 186 HV hardness after aging while the vacuum cast system shows a hardness of almost 300 HV. fracture toughness at reduced temperature shows only small changes, with the vacuum cast sample at -40C showing only a 15 J difference while previously in the homogenized state an increase of 26 J was shown to happen at reduced temperature.

Table 9. Shows the fracture toughness of both the vacuum induction cast samples and the foundry cast samples. The small difference in Ti/Al shows a change of 100 HV in terms of hardness as well as a 120J fracture toughness difference in the homogenized state as well as 60J difference in the aged state. Little change is observed from testing at -40C

Processing Condition	Testing Temperature	Foundry Cast	Hardness (HV)	Vacuum Cast	Hardness (HV)
Homo	RT	118 ± 24	127 ± 6	215 ± 8	115 ± 3
	-40C	124 ± 12	124 ± 2	241 ± 5	112 ± 2
Aged	RT	11 ± 3	186 ± 7	83 ± 2	292 ± 4
	-40C	8 ± 0.9	183 ± 3	68 ± 2	303 ± 3

3.2.2. Tensile Testing. Tensile test results is shown in figure 6. Notably, the vacuum cast samples have a significantly higher ductility of 45% in the homogenized state and 43% in the aged state while in comparison. The foundry cast homogenized system exhibits the same ultimate tensile strength (UTS) as the vacuum cast system, though at a reduced ductility of 30%. The difference between the vacuum cast aged and

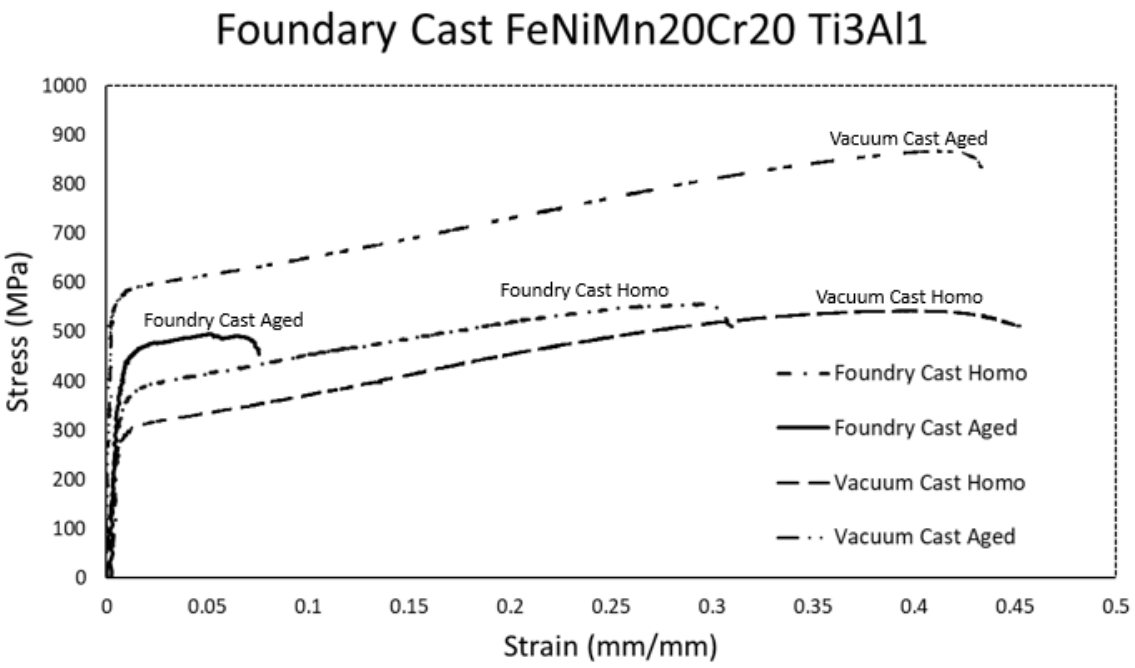

Figure 6. Shows the difference of the VIM cast system vs the foundry cast alloy. The VIM cast system after aging shows a YS of 590 MPa and a UTS of 890 MPa at an elongation of 44%. The foundry cast system shows a peak strength in its homogenized state at 525 MPa at an elongation of 30%. The aged foundry cast system shows a higher YS by about 100 MPa at 450 MPa but shows only 7% elongation with a UTS at 485 MPa.

homogenized is also evident in the yield strength (YS) with a difference of 300 MPa from 290 MPa to 587 MPa in the aged sample. The foundry cast aged system exhibits the least ductility at only 8% and while a higher YS of 453 MPa can be observed. The UTS is

slightly lower than that of the foundry cast homogenized system at only 492 MPa which is similar to that of the vacuum cast homogenized system. Finally, the vacuum cast homogenized system shows a UTS of 880 MPa which is a significant change over the UTS of all other systems.

4. DISCUSSION

4.1. EXPERIMENTAL TESTING AND PROCEDURE

4.1.1. Vacuum Induction. The use of the vacuum induction furnace, especially the setup used in this work, does not allow for easy access to sampling nor temperature regulation. These factors, as well as the addition of all elements initially can be linked to the reduction of alloying elements as well as Mn in the final product. Due to the lack of temperature control, higher temperatures must have been reached, resulting in the off gassing of Mn oxide. Presumably, this occurrence proceed the large amount of green/grey vapor that formed during the casting process, which is also seen in casting in the foundry though in a reduced amount. The addition of the Ti and Al initially also allows any inclusions to form early on and allows these to form in the slag layer. While the slag layer is significantly reduced in size as well as thickness a thin layer is present in all castings in this vacuum induction furnace. Additionally, the increased Al is most likely due to interactions of the melt with the Al2O3 crucible.

4.1.2. Foundry Induciton Furnace. The foundry induction furnace casting showed that, using modern steel casting techniques, it is possible to cast high entropy alloys. While some work is required to refine the amount of pickup there is for alloying

elements Ti and Al, the late addition of these elements into the melt is crucial to reduce the amount of loss to slag formation. This is especially important as these elements readily form slags and is reinforced by their use as oxygen getter elements in many processes. The high Al pickup was due to the late addition of Al in the ladle rather than the furnace and the Ti having taken up much of the oxygen in the melt.

A constant argon flow of 0.3L/m for a protective atmosphere is also a requirement as N and O from atmosphere is introduced into the melt. In the case of this casting, most of the oxygen seems to originate from the Ti itself, suggesting that the raw material had a large amount of oxide already formed. This emphasizes the need for raw materials to be especially considered. In the case of this casting, “sponge” titanium was used, which has an extremely high surface area and potentially large amounts of entrapped gas which is released into the melt during the melting process. Short of these alloying elements though, few hurdles arose which can not easily be handled with standard casting procedures.

4.2. INCLUSIONS

Inclusions in the foundry system traces back to specific processing conditions; while Al was added, few to no inclusions were found to contain excess Al.

4.2.1. Ti Addition. The Ti addition in both melts resulted in a high TiN content. Though both systems experienced this growth, the focus will be on the foundry cast system. The addition of Ti lead to a significant reduction, almost 0.04 volume fraction in oxides. Such reduction can be directly attributed to the Ti addition as the de-slag procedures had not begun nor had any slag layer been removed. Thus, it is reasonable to assume that the Ti took the oxygen from the melt or other oxides and entered the slag

layer as a Ti-oxide as is common when using Ti as an oxygen getter during casting. Ti can also be seen to draw out S from the melt in the form of Ti-sulfides reducing the number of Mn-sulfides found though Mn-sulfides were still present.

4.2.2. Filter. The data in table 7 reflects the use of a filter in castings, insofar as the filter shows its effectiveness in reducing all forms of inclusions. While no filter was used for the vacuum induction furnace castings, filters, common in steel castings, are an absolute necessity for the many different inclusions found in high entropy alloys.

4.2.3. Atmospheric Control. While atmospheric control is not necessarily easy, a strong emphasis should be placed on atmospheric control. The difference between the vacuum induction furnace and the foundry induction furnace draws a strong parallel: with a minimum factor of 10 reduction in inclusion volume fraction between the high atmospheric control vacuum induction furnace and the foundry induction furnace the atmospheric controls are necessary and should be emphasized.

4.3. MECHANICAL TESTING

Mechanical testing highlighted the difference between each casting. Due to differences in the composition, no conclusions can be drawn on the effect of inclusions on the mechanical properties beyond that inclusions are known to negatively impact mechanical properties. The difference in mechanical properties, however, can be highlighted, and even slight differences in alloying elements can result in marked differences in both strength and ductility. The difference in precipitates between the aged foundry cast system and the aged vacuum cast system is also highlighted though precipitate analysis is beyond the scope of this work. In addition, fracture toughness data clearly shows the effect of the compositional differences.

5. CONCLUSION

In this work, the scalability of high entropy alloy castings was investigated. The work showed that, while compositional differences may occur and dialing in of the composition will have to occur, this is not outside the realm of specialty steel manufacturing. Using a common steel procedure and using modern steel casting technologies, a high entropy alloy: FeNiMn20Cr20 Ti1Al3 was cast. While increased inclusions are present due to a lower atmosphere control in the foundry cast system, the overall low amount of inclusions suggests that modern steel casting techniques are more than capable of handling the casting of high entropy alloys.

APPENDIX A.

AVERAGE MISSORIENTATION MAP

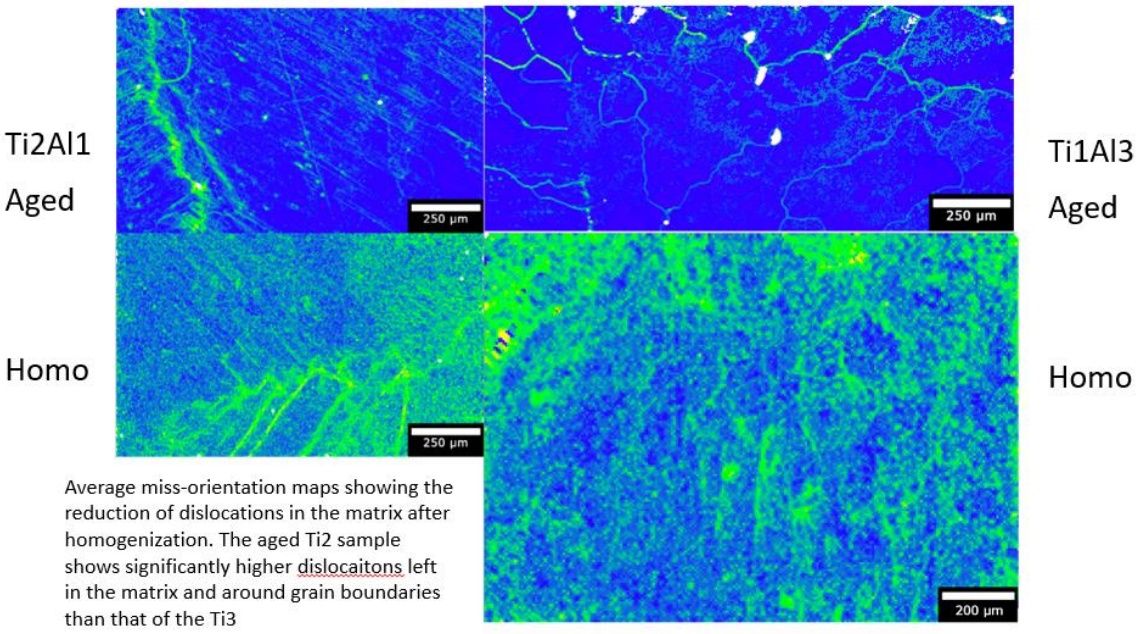

Appendix A. 1. Shows the average missorientation mapping of the Ti2 and Al3 systems pre and post homogenized.

APPENDIX B.

A HIGH RESOLUTION IMAGE OF THE FRACUTURE SURFACE OF Ti_3Al_1

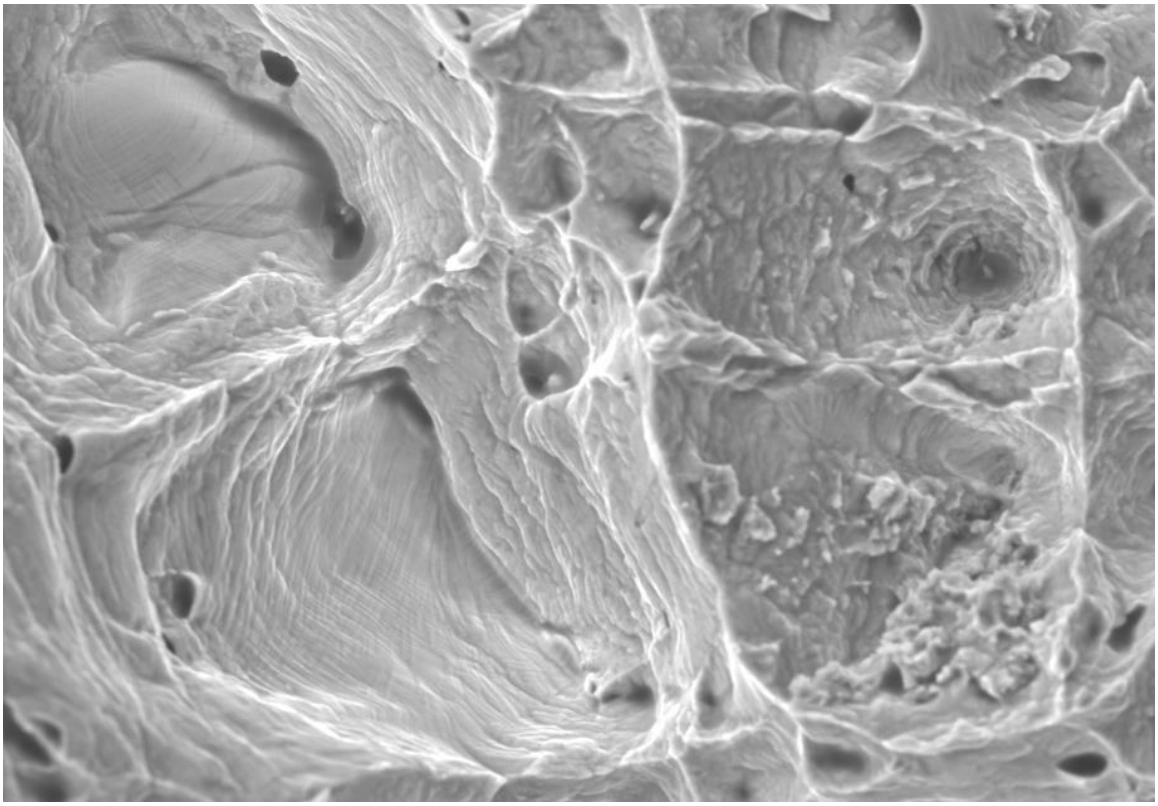

Figure B.1. Shows the fracture surface of the Al3 system. Some slip plane activation is visible on the fracture surface.

APPENDIX C.

SHOWS THE CLOSE UP OF THE FRACTURE SURFACE OF THE Ti_2Al_1 SYSTEM

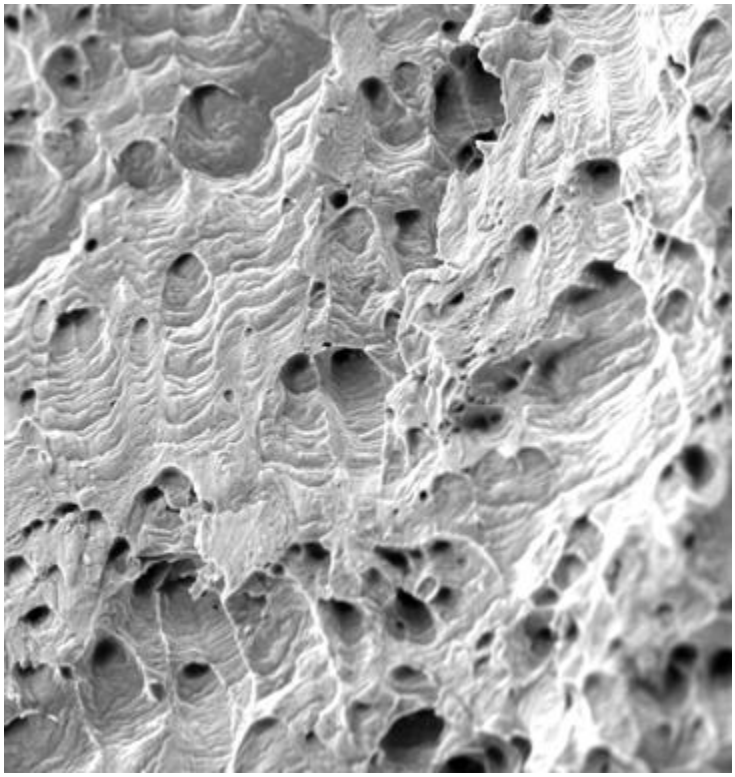

Appendix C.1. Shows the Ti2 fracture surface showing a relatively ductile fracture with many small inclusions acting as fracture initiation sites.

REFERENCES

1. Huang, KH JY (Hsinchu: NTHU. A study on the multicomponent alloy systems containing equal-mole elements. 1996.

2. Cantor B, Chang ITH, Knight P, Vincent AJB. Microstructural development in equiatomic multicomponent alloys. Mater Sci Eng A. 2004;375–377(1-2 SPEC. ISS.):213–218. https://doi.org/10.1016/j.msea.2003.10.257

3. Radis R, Zickler GA, Stockinger M, Sommitsch C, Kozeschnik E. Numerical simulation of the simultaneous precipitation of δ and γ′ phases in the Ni-base superalloy ATI Allvac®718 PlusTM. 7th Int Symp Superalloy 718 Deriv 2010. 2010;2:569–578. https://doi.org/10.1002/9781118495223.ch44

4. Dasari S, Jagetia A, Chang YJ, et al. Engineering multi-scale B2 precipitation in a heterogeneous FCC based microstructure to enhance the mechanical properties of a Al0.5Co1.5CrFeNi1.5 high entropy alloy. J Alloys Compd. 2020;830:154707. https://doi.org/10.1016/j.jallcom.2020.154707

5. Shi T, Lei PH, Yan X, et al. Current development of body-centered cubic high-entropy alloys for nuclear applications. Tungsten. 2021;3(2):197–217. https://doi.org/10.1007/s42864-021-00086-6

6. Chen ST, Tang WY, Kuo YF, et al. Microstructure and properties of age-hardenable AlxCrFe1.5MnNi0.5 alloys. Mater Sci Eng A. 2010;527(21–22):5818–5825. https://doi.org/10.1016/j.msea.2010.05.052

7. Riznyk S, Artushenko A. Aeroengine high pressure turbine blade cooling system concept. Proc ASME Turbo Expo. 2013;3. https://doi.org/10.1115/GT2013-95789

8. Shi Y, Yang B, Liaw PK. Corrosion-resistant high-entropy alloys: A review. Metals (Basel). 2017;7(2):1–18. https://doi.org/10.3390/met7020043

9. Langner J, Piekoszewski J, Werner Z, et al. Surface modification of constructional steels by irradiation with high intensity pulsed nitrogen plasma beams. Surf. Coatings Technol. 2000 https://doi.org/10.1016/S0257-8972(00)00616-2

10. Tsai MH, Yeh JW. High-entropy alloys: A critical review. Mater Res Lett. 2014;2(3):107–123. https://doi.org/10.1080/21663831.2014.912690

11. Miracle DB, Senkov ON. A critical review of high entropy alloys and related concepts. Acta Mater. 2017. https://doi.org/10.1016/j.actamat.2016.08.081

12. Rao JC, Diao HY, Ocelík V, et al. Secondary phases in AlxCoCrFeNi high-entropy alloys: An in-situ TEM heating study and thermodynamic appraisal. Acta Mater. 2017;131:206–220. https://doi.org/10.1016/j.actamat.2017.03.066

13. Lee C, Song G, Gao MC, et al. Lattice distortion in a strong and ductile refractory high-entropy alloy. Acta Mater. 2018;160:158–172. https://doi.org/10.1016/j.actamat.2018.08.053

14. Chen L, Li Z, Dai P, Fu P, Chen J, Tang Q. Effects of carbon addition on microstructure and mechanical properties of Fe50Mn30Co10Cr10high-entropy alloy prepared by powder metallurgy. J Mater Res Technol. 2022;20:73–87. https://doi.org/10.1016/j.jmrt.2022.07.067

15. Wu J, Liu X, Zhu H. Achieving strength-ductility balance in a casting non-equiatomic FeCoNi based medium-entropy alloy via Al and Ti combination addition. J Mater Res Technol. 2023;23:627–636. https://doi.org/10.1016/j.jmrt.2023.01.035

16. Svoboda J, Fischer FD, Riedel H, Kozeschnik E. Precipitate growth in multi-component systems with stress relaxation by diffusion and creep. Int J Plast. 2016;82:112–126. https://doi.org/10.1016/j.ijplas.2016.03.001

17. Tsai CW, Chen YL, Tsai MH, Yeh JW, Shun TT, Chen SK. Deformation and annealing behaviors of high-entropy alloy Al0.5CoCrCuFeNi. J Alloys Compd. 2009. https://doi.org/10.1016/j.jallcom.2009.06.182

18. Zhang Y, Zhou YJ, Lin JP, Chen GL, Liaw PK. Solid-solution phase formation rules for multi-component alloys. Adv Eng Mater. 2008;10(6):534–538. https://doi.org/10.1002/adem.200700240

19. Wu Z, Bei H. Microstructures and mechanical properties of compositionally complex Co-free FeNiMnCr18 FCC solid solution alloy. Mater Sci Eng A. 2015;640:217–224. https://doi.org/10.1016/j.msea.2015.05.097

20. Kumar NAPK, Li C, Leonard KJ, Bei H, Zinkle SJ. Microstructural stability and mechanical behavior of FeNiMnCr high entropy alloy under ion irradiation. Acta Mater. 2016;113:230–244. https://doi.org/10.1016/j.actamat.2016.05.007

21. Li R, Zhang W, Zhang Y, Liaw PK. The effects of phase transformation on the microstructure and mechanical behavior of FeNiMnCr.75Alx high-entropy alloys. Mater Sci Eng A. 2018;725(April):138–147. https://doi.org/10.1016/j.msea.2018.04.007

SECTION

2. CONCLUSIONS AND RECOMMENDATIONS

2.1. CONCLUSIONS

Two high entropy alloys were developed and processed. Initial success in processing showed the processing of high entropy alloys resulted in similar results as found in steels in both grain size reduction and increase in strength. Further work showed that the use of precipitation strengthening especially focusing on γ' is an effective means of strengthening alloys.

Ti and Al were investigated to determine their effectiveness as strengthening agents following literature. The ratio of Ti to Al is a vital number that must be kept in mind. While γ' still forms, the size and morphology of the precipitates changes drastically based on the ratio with more Al showing a more distributed smaller γ' formation. With the base alloy $FeNiMn_{20}Cr_{20}$ and a Ti and Al ratio of 1:3 and aged at 750C for a minimum of 1.5 hours an improvement of almost 300 MPa can be achieved as with only a 1% loss in elongation. This opens the possibility of achieving increased strength as little to no reduction of elongation, a touted tenant, the achievement of one without reduction in the other, of high entropy alloys.

The scaling of high entropy alloys was also investigated. Through the use of modern steel casting techniques, it was investigated if high entropy alloys could be simply cast or if more complex means of production would need to be employed. Though not equivalent to the vacuum induction melting process, a high entropy alloy was

successfully cast and though refining of the processes is necessary, the final product showed that existing casting methods are more than capable of producing high entropy alloys. This suggests that the scaling of high entropy alloys can move forward using existing infrastructure, significantly reducing the potential costs of large-scale high entropy alloy production.

It should be noted that a major hurdle of casting high entropy alloys in “standard” induction furnace setups with only a protective gas made of flowing argon gas runs the risk of creating a complex group of inclusions. In steel, many of the inclusions are relatively simple, but due to the nature of high entropy alloys with multiple principal elements a wider variety of inclusions may form. In addition, the processing methods may have a large effect on the reduction of the inclusions with some inclusions almost completely disappearing based on based on simple thermal treatments while unexpected inclusions can pop up.

In summary, precipitation strengthened high entropy alloys in conjunction with the processing of rolling shows the capability to become a strong easily scalable material. The strengthening effect of precipitation strengthening and processing allows for the possibility of a high entropy alloy moving forward to the consumer market as a when rather than an if.

2.2. RECOMMENDATIONS

The high entropy alloys studied here have been shown to behave much like steels in both processing as well as precipitation and casting. With these factors in mind, the

move forward to design practical high entropy alloys ready for production environments can move forward. A greater understanding of precipitation is still required but scalability of high entropy alloys has been shown to be an achievable goal.

BIBLIOGRAPHY

1. Cantor B, Chang ITH, Knight P, Vincent AJB. Microstructural development in equiatomic multicomponent alloys. Mater Sci Eng A. 2004;375–377(1-2 SPEC. ISS.):213–218. https://doi.org/10.1016/j.msea.2003.10.257

2. Yeh JW, Chen SK, Lin SJ, et al. Nanostructured high-entropy alloys with multiple principal elements: Novel alloy design concepts and outcomes. Adv Eng Mater. 2004;6(5):299-303+274. https://doi.org/10.1002/adem.200300567

3. B.S. Murty, Jien-Wei Yeh, S. Rananathan PPB. High-Entropy Alloys. n.d.

4. Liu WH, Lu ZP, He JY, et al. Ductile CoCrFeNiMox high entropy alloys strengthened by hard intermetallic phases. Acta Mater. 2016;116:332–342. https://doi.org/10.1016/j.actamat.2016.06.063

5. Qi YL, Zhao L, Sun X, et al. Enhanced mechanical performance of grain boundary precipitation-hardened high-entropy alloys via a phase transformation at grain boundaries. J Mater Sci Technol. 2021;86:271–284. https://doi.org/10.1016/j.jmst.2021.01.061

6. He JY, Wang H, Huang HL, et al. A precipitation-hardened high-entropy alloy with outstanding tensile properties. Acta Mater. 2016;102:187–196. https://doi.org/10.1016/j.actamat.2015.08.076

7. Gludovatz B, Hohenwarter A, Catoor D, Chang EH, George EP, Ritchie RO. A fracture-resistant high-entropy alloy for cryogenic applications. Science (80-). 2014;345(6201):1153–1158. https://doi.org/10.1126/science.1254581

8. Sebeck K, Toppler I, Rogers M, et al. High Mn, High Al Steels for Thick Plate Armor Applications. Gvsets 2018. 2018.

9. Edmondson PD, Briggs SA, Yamamoto Y, et al. Irradiation-enhanced α′ precipitation in model FeCrAl alloys. Scr Mater. 2016;116:112–116. https://doi.org/10.1016/j.scriptamat.2016.02.002

10. Jiang G, Xu D, Feng P, Guo S, Yang J, Li Y. Corrosion of FeCrAl alloys used as fuel cladding in nuclear reactors. J Alloys Compd. 2021;869:159235. https://doi.org/10.1016/j.jallcom.2021.159235

11. Sun Z, Yamamoto Y, Chen X. Impact toughness of commercial and model FeCrAl alloys. Mater Sci Eng A. 2018;734(July):93–101. https://doi.org/10.1016/j.msea.2018.07.074

12. Tsai MH, Yeh JW. High-entropy alloys: A critical review. Mater Res Lett. 2014;2(3):107–123. https://doi.org/10.1080/21663831.2014.912690

13. Miracle DB, Senkov ON. A critical review of high entropy alloys and related concepts. Acta Mater. 2017;122:448–511. https://doi.org/10.1016/j.actamat.2016.08.081

14. Mansoori GA, Carnahan NF, Starling KE, Leland TW. Equilibrium thermodynamic properties of the mixture of hard spheres. J Chem Phys. 1971;54(4):1523–1526. https://doi.org/10.1063/1.1675048

15. Song H, Tian F, Hu QM, et al. Local lattice distortion in high-entropy alloys. Phys Rev Mater. 2017;1(2):1–8. https://doi.org/10.1103/PhysRevMaterials.1.023404

16. Lee C, Song G, Gao MC, et al. Lattice distortion in a strong and ductile refractory high-entropy alloy. Acta Mater. 2018;160:158–172. https://doi.org/10.1016/j.actamat.2018.08.053

17. Tsai KY, Tsai MH, Yeh JW. Sluggish diffusion in Co-Cr-Fe-Mn-Ni high-entropy alloys. Acta Mater. 2013;61(13):4887–4897. https://doi.org/10.1016/j.actamat.2013.04.058

18. Li Q, Chen W, Zhong J, Zhang L, Chen Q, Liu ZK. On sluggish diffusion in FCC Al–Co–Cr–Fe–Ni high-entropy alloys: An experimental and numerical study. Metals (Basel). 2018;8(1). https://doi.org/10.3390/met8010016

19. Divinski S V., Pokoev A V., Esakkiraja N, Paul A. A Mystery of "Sluggish Diffusion" in High-Entropy Alloys: The Truth or a Myth? Diffus Found. 2018;17:69–104. https://doi.org/10.4028/www.scientific.net/df.17.69

20. Liu YX, Cheng CQ, Shang JL, Wang R, Li P, Zhao J. Oxidation behavior of high-entropy alloys AlxCoCrFeNi (x=0.15, 0.4) in supercritical water and comparison with HR3C steel. Trans Nonferrous Met Soc China (English Ed. 2015;25(4):1341–1351. https://doi.org/10.1016/S1003-6326(15)63733-5

21. Uberuaga BP, Vernon LJ, Martinez E, Voter AF. The relationship between grain boundary structure, defect mobility, and grain boundary sink efficiency. Sci Rep. 2015;5:1–9. https://doi.org/10.1038/srep09095

22. Wilson JA, Evitts LJ, Rushton MJD, Middleburgh SC, Lee WE. High entropy alloys for accident tolerant fuel applications HIGH ENTROPY ALLOYS FOR ACCIDENT TOLERANT FUEL APPLICATIONS. 2022;(June 2021).

23. Bian BB, Guo N, Yang HJ, et al. A novel cobalt-free FeMnCrNi medium-entropy alloy with exceptional yield strength and ductility at cryogenic temperature. J Alloys Compd. 2020;827:1–7. https://doi.org/10.1016/j.jallcom.2020.153981

24. Rao JC, Diao HY, Ocelík V, et al. Secondary phases in AlxCoCrFeNi high-entropy alloys: An in-situ TEM heating study and thermodynamic appraisal. Acta Mater. 2017;131:206–220. https://doi.org/10.1016/j.actamat.2017.03.066

25. W.E. Luecke et al. Mechanical properties of structural steels. Natl Institude Stand Technol. 2005;1–288.

26. Scales M, Anderson J, Kornuta JA, Switzner N, Gonzalez R, Veloo P. Accurate Estimation of Yield Strength and Ultimate Tensile Strength through Instrumented Indentation Testing and Chemical Composition Testing. Materials (Basel). 2022;15(3). https://doi.org/10.3390/ma15030832

27. Yang T, Zhao Y, Liu W, Kai J, Liu C. L12-strengthened high-entropy alloys for advanced structural applications. J Mater Res. 2018;33(19):2983–2997. https://doi.org/10.1557/jmr.2018.186

28. Sakai T, Belyakov A, Kaibyshev R, Miura H, Jonas JJ. Dynamic and post-dynamic recrystallization under hot, cold and severe plastic deformation conditions. Prog Mater Sci. 2014;60(1):130–207. https://doi.org/10.1016/j.pmatsci.2013.09.002

29. Guo L, Ou X, Ni S, Liu Y, Song M. Effects of carbon on the microstructures and mechanical properties of FeCoCrNiMn high entropy alloys. Mater Sci Eng A. 2019;746(January):356–362. https://doi.org/10.1016/j.msea.2019.01.050

30. Zhang Y, Zuo TT, Tang Z, et al. Microstructures and properties of high-entropy alloys. Prog Mater Sci. 2014;61(September 2013):1–93. https://doi.org/10.1016/j.pmatsci.2013.10.001

31. Ming K, Bi X, Wang J. Precipitation strengthening of ductile Cr15Fe20Co35Ni20Mo10 alloys. Scr Mater. 2017;137:88–93. https://doi.org/10.1016/j.scriptamat.2017.05.019

32. Martin JW. Precipitation Hardening: Theory and Applications. 1998;1–224.

33. Ayyagari A V., Gwalani B, Muskeri S, Mukherjee S, Banerjee R. Surface degradation mechanisms in precipitation-hardened high-entropy alloys. npj Mater Degrad. 2018;2(1). https://doi.org/10.1038/s41529-018-0054-1

34. Liu WH, Yang T, Liu CT. Precipitation hardening in CoCrFeNi-based high entropy alloys. Mater Chem Phys. 2018;210:2–11. https://doi.org/10.1016/j.matchemphys.2017.07.037

35. Chen D, He F, Han B, et al. Synergistic effect of Ti and Al on L12-phase design in CoCrFeNi-based high entropy alloys. Intermetallics. 2019;110(May):106476. https://doi.org/10.1016/j.intermet.2019.106476

36. Radis R, Zickler GA, Stockinger M, Sommitsch C, Kozeschnik E. Numerical simulation of the simultaneous precipitation of δ and γ′ phases in the Ni-base superalloy ATI Allvac®718 PlusTM. 7th Int Symp Superalloy 718 Deriv 2010. 2010;2:569–578. https://doi.org/10.1002/9781118495223.ch44

37. Wu Z, Bei H. Microstructures and mechanical properties of compositionally complex Co-free FeNiMnCr18 FCC solid solution alloy. Mater Sci Eng A. 2015;640:217–224. https://doi.org/10.1016/j.msea.2015.05.097

38. Luebbe M, Duan J, Zhang F, et al. A high-strength precipitation hardened cobalt-free high-entropy alloy. Mater Sci Eng A. 2023;870(February):144848. https://doi.org/10.1016/j.msea.2023.144848

39. Kumar NAPK, Li C, Leonard KJ, Bei H, Zinkle SJ. Microstructural stability and mechanical behavior of FeNiMnCr high entropy alloy under ion irradiation. Acta Mater. 2016. https://doi.org/10.1016/j.actamat.2016.05.007

VITA

Hans Jakob Pommerenke earned a Bachelor of Science degree in Ceramic Engineering in 2018, followed by a Doctor of Philosophy degree in Material Science and Engineering obtained in May 2024.

From 2019 to 2023, Pommerenke served as a Graduate Research Assistant at Missouri University of Science and Technology. In this capacity, he honed his academic and research skills while demonstrating a keen aptitude for critical thinking. His primary responsibilities included creating innovative high entropy alloys, utilizing advanced analytical techniques such as SEM, EDS, EBSD, TEM, and STEM for sample characterization. Additionally, Pommerenke played a pivotal role in designing and fabricating testing equipment, ranging from larger scale mechanical testing setups to miniature systems tailored for sub-sized specimens. He also took on a teaching role, instructing students in various mechanical testing techniques and aiding in the interpretation and processing of resulting data. Through these experiences, Pommerenke collaborated extensively with colleagues and established himself as a subject matter expert in the realm of mechanical testing.

Parallel to his academic pursuits, Pommerenke was actively engaged in Design Teams from 2014 to 2022. Notably, he had led the composites group for the Missouri University Formula SAE team, overseeing the design and production of carbon fiber and fiberglass components for race cars during the 2015 and 2016 seasons. Working within a multidisciplinary team, Pommerenke capitalized on the diverse expertise of his peers to achieve success in crafting competitive race cars.